Integral Field Spectroscopy of Optical Recombination Lines in the Planetary Nebula NGC 7009: Implications for Dual-Abundance Models

by

Sehyun Hwang, B.S.

THESIS

Presented to the Faculty of the Graduate School of

The University of Texas at Austin

in Partial Fulfillment

of the Requirements

for the Degree of

MASTER OF ARTS

THE UNIVERSITY OF TEXAS AT AUSTIN

August 2009

Integral Field Spectroscopy of Optical Recombination Lines in the Planetary Nebula NGC 7009: Implications for Dual-Abundance Models

APPROVED BY

SUPERVISING COMMITTEE:

Harriet L. Dinerstein, Supervisor

John H. Lacy

Gregory A. Shields

Dedicated to my parents, Mr. Wonchul and Mrs. Wooboon Hwang

Acknowledgments

I would like to express my deepest gratitude to my adviser, Dr. Harriet L. Dinerstein, for her continuous support and guidance throughout the completion of this study. Were it not for her valuable teaching both in academics and in everyday life, the completion of this thesis would not have been possible.

I am also highly grateful for the help of the other members of my committee, Gary J. Hill, John H. Lacy, and Gregory A. Shields, whose collective comments and questions have greatly improved the presentation of this work, and my understanding of the material.

I thank Joshua J. Adams and Guillermo A. Blanc very much for their help on the observations and the data reduction.

The coffee time with my awesome friends, Masatoshi Shoji, Donghui Jeong, and Hyo Jeong Kim always has been a big pleasure to me.

Finally, I would like to thank to my family, my parents and my brother Joonghyun Hwang, with endless love and gratitude.

This research was supported by NSF grants AST 0408609 and 0708245 to Harriet L. Dinerstein, and the VIRUS-P has been made possible by a generous donation from the Cynthia and George Mitchell Foundation.

Integral Field Spectroscopy of Optical Recombination Lines in the Planetary Nebula NGC 7009: Implications for Dual-Abundance Models

Sehyun Hwang, M.A.
The University of Texas at Austin, 2009

Supervisor: Harriet L. Dinerstein

We have investigated the spatial distribution of the optical recombination lines (ORLs) in the planetary nebula NGC 7009, utilizing the integral field spectrograph Visible Integral-field Replicable Unit Spectrograph-Prototype (VIRUS-P) on the McDonald Observatory 2.7-m telescope, in order to study the abundance discrepancy problem and probe the currently popular dual-abundance model. Spectra were obtained over the wavelength range $\lambda\lambda$ 3550-5850 with a spectral resolution of FWHM$\sim 5\mathring{A}$, across the full VIRUS-P sampling field (112×112-$arcsec^2$) with an angular resolution of $4''.1$ per fiber. Several O II ORLs were detected in 41 VIRUS-P fiber positions, along with recombination and collisionally excited lines of other ions. In order to measure the O II ORLs, which typically have fluxes a mere 0.1-0.01 % that of Hβ, we subtracted the nebular continuum emission before fitting and deblending the O II line fluxes. We determined O^{2+}/H^{+} ORL abundances from five O II ORLs:

i.e. the 4f-3d transitions $\lambda\lambda$4089, 4275, 4282, 4303, and the 3p-3s transition λ4676. The C^{2+}/H^{+}, He^{+}/H^{+}, He^{2+}/H^{+} abundances were derived from ratios among C II λ4267, He I λ4471, He II λ4686, and Hβ λ4861. We present maps of the ORL-based abundances and derive empirical radial gradients in the O^{2+}/H^{+} and C^{2+}/H^{+} ORL abundances, which peak toward the central star. In the context of the dual-abundance model, this would indicate a central concentration in the distribution of the posited cold, hydrogen-deficient and metal-rich inclusions. The O^{2+}/H^{+} and C^{2+}/H^{+} ORL abundances are positively correlated, and we found marginal evidence, based on correlations with He^{2+}/He, that the cold, metal-rich inclusions might be associated with high ionization regions. The O^{2+}/H^{+} forbidden line-based abundance was determined from the [O III] λ4363 collisionally excited line (CEL) with a radially varying T_e. The resulting abundance discrepancy factor (ADF) was obtained for each fiber, and the radially increasing ADFs toward the NGC 7009 central star also indicate a centrally concentrated distribution of the postulated cold component.

We examined possible sets of physical conditions in the cold, metal-rich inclusions. An extremely low T_e(O II ORL) of $\sim$300K was derived from the observed intensity ratio I(λ4676)/I(λ4089), with no significant spatial variations across the nebula. Consistent values of n_e and O/H abundance abundance were constrained using the photoionization model Cloudy. For these physical conditions, we also calculated the volume filling factor and mass fraction of cold gas. A possible set of parameters consistent with the data is $T_e\sim$350K,

$n_e \sim 3 \times 10^4 cm^{-3}$, and an O/H value of $\sim$100$\times$solar for the inclusions. Based on the observed correlation between the C II and O II ORLs, the C/H abundance would have to be enhanced by a similar factor as O/H in the cold component.

Table of Contents

Chapter 1

Introduction

1.1 The Puzzle of the Optical Recombination Lines (ORLs)

Traditionally, the collisionally excited lines (CELs, often referred to as "forbidden" lines) have been used to measure the elemental abundances in the planetary nebulae (PNe) since they are very bright and prominent emission features. The strength of the CELs, however, depends strongly upon the electron temperature, T_e, and hence the abundances derived from the CELs are very sensitive to uncertainties in the value of T_e and to temperature variations of a nebula. In other words, the presence of spatial variations or fluctuations in T_e can cause systematic underestimates of the CEL-based abundances (Peimbert et al. 1995; Mathis 1995). An alternate approach for abundance determinations of heavy elements such as O relative to H, is to use the optical recombination lines (ORLs, or "permitted" lines) which are produced by the recombination cascade (Peimbert, Storey, and Torres-Peimber 1993; Liu et al. 1995). The intrinsic advantage of ORLs over conventional CELs is that the ORL abundance relative to hydrogen is essentially free of uncertainties caused by temperature variations because the temperature dependences of some ORLs and the H I recombination lines are so similar that they virtually cancel out (e.g. O II ORL λ4649 and Hβ; Liu 2006a). Accordingly, the ORLs should pro-

vide T_e-independent abundance determinations, although most ORLs are very weak, with typically about 0.1 to 0.01 per cent of the flux of Hβ (Peimbert, Storey, and Torres-Peimber 1993).

A currently intriguing problem in PNe is the discrepancy between abundances determined from ORLs and CELs (Liu et al. 1995, 2000; Garnett and Dinerstein 2001; Peimbert et al. 2004; Tsamis et al. 2004, 2008). In many PNe (not all though) the weak ORLs tend to yield systematically higher abundances in some heavy elements (notably oxygen, carbon, nitrogen, and neon) compared to those from the bright CELs, even though the elemental abundances derived from two different types of emission lines in the same ion of the same element should match. This disparity is quantified in terms of an abundance discrepancy factor (ADF), defined as the ratio of ionic abundances determined from the ORLs to those derived from the CELs for the same ion (Tsamis et al. 2004). For about 90 PNe studied using ORLs obtained from deep long-slit spectroscopy up to date, the ADFs often go up to 2-3, and even higher for some PNe (Tsamis et al. 2004; Wesson et al. 2005). One of the most extreme ADF values, >70, was found for the southern planetary nebula PN Hf 2-2 (Liu et al. 2006b).

The size of the ADFs varies not only from nebula to nebula but also with spatial positions within one nebula (Garnett and Dinerstein 2001; Tsamis et al. 2008). In addition, the abundance discrepancy between ORL and CEL in PNe has been commonly observed in second-row element ions (e.g. O^{2+}, C^{2+}, N^{2+}, Ne^{2+}), but not for magnesium, one of the third-row elements stud-

ied with an ORL (Barlow et al. 2003, Liu et al. 2004). There is some possible evidence that the abundance discrepancy might be related to the difference in electron temperatures measured from CEL line ratios (e.g. [O III] $\lambda\lambda(5007{+}4959)/\lambda 4363$) and from recombination diagnostics (e.g. H I Balmer jump (BJ), He I recombination line ratio: Peimbert 1971; Barker 1978; Liu and Danziger 1993; Liu et al. 2000, 2001, 2003; Liu et al. 2004; Tsamis et al. 2004; Wesson et al. 2005).

These discrepancies are of concern not only as a curiosity, but because they call into question the nebular abundances determined from standard procedures. Peimbert et al. (1993, 2004), based on the earlier concept of a dispersion in temperature parameterized by a temperature fluctuation parameter t^2 (Peimbert 1967), ascribed the abundance discrepancy to a thermally inhomogeneous structure within a nebula. They showed that the derived ADF(O^{2+}) values in NGC 6572 and NGC 5315 could be explained with t^2 parameters of 20% and 23% respectively. Alternatively, Rubin (1989) and Viegas and Clegg (1994) suggested that dense clumps with high electron densities ($n_e \gtrsim 10^6 cm^{-3}$) can cause significant overestimation of T_e(CEL), by collisionally suppressing CELs with relatively low critical densities, and consequently lead to an underestimation of the abundance. Note that both the temperature fluctuations and density inhomogeneities explanations attribute the apparent abundance discrepancies to underestimation of the CEL abundances. In either case, the higher values derived from ORLs would be the *true* abundances. Also, each of these explanations predicts certain trends: i.e. dependence of the abundance

discrepancies on the excitation energy (for t^2) or the critical density (for dense clumps). That is, the underestimation of the CEL-based abundances would become more severe when measured from forbidden lines with higher excitation energy (in temperature fluctuations model) or lower critical density (in the density inhomogeneities model). However, Tsamis et al. (2004) and Liu et al. (2004) found that the magnitude of the ADFs remains rather uniform for many different diagnostic UV, optical, far-IR CELs from a large number of PNe and concluded that neither temperature fluctuations or density inhomogeneities is a sufficient solution. Moreover, nebular photoionization models do not predict the large temperature fluctuations which are required to resolve ADFs of 2 or higher (Gruenwald and Viegas 1995; Kingdon and Ferland 1995).

1.2 The Dual Abundance Model

The "dual-abundance model" was first proposed by Liu et al. (2000). This picture postulates that there are cold, hydrogen-deficient and metal-rich inclusions embedded in ambient, hot gas with "normal" chemical composition (i.e. $\sim$solar). These cold inclusions constitute only a small fraction of the volume and mass of the nebula. In the dual-abundance model, the cold, metal-rich inclusions are primarily responsible for the enhanced ORL fluxes (due to the large chemical enrichments and the inversely proportional power-law dependence of the radiative recombination coefficients on T_e, in spite of the small filling factors within a given nebula), while their contribution to the CEL flux would be negligible. In contrast, the ambient, hot gas with normal

chemical composition (that occupies most of the volume) dominates the fluxes of most CELs because the emissivities of forbidden lines have strong positive exponential dependences on T_e. In this paradigm, the ORL/CEL abundance discrepancy is an artifact, arising from the failure to consider the two components separately. The dual-abundance model is thus a fundamentally different approach to the ADF problem, compared to the previously suggested temperature fluctuations or density inhomogeneities, since it ascribes the ORL/CEL abundance discrepancies to enriched ORL abundances, rather than underestimated CEL abundances. In this vein, the analysis of the heavy element ORLs is of paramount importance to characterize the physical properties of the cold and hydrogen-deficient component, if they *do* exist.

Under the dual-abundance model, there should be differences in the values derived from various temperature diagnostics, in particular T_e(ORLs)$\leqslant$ T_e(He I)$\leqslant$ T_e(H I BJ)$\leqslant$ T_e([O III] CELs) (Liu 2003). This behavior is seen in many PNe with significant ADFs (Liu et al. 2004; Tsamis et al. 2004; Wesson et al. 2005). In such PNe, the diagnostic O II recombination line ratios indicate very low electron temperatures, $T_e \lesssim 10^3 K$, which would be a natural consequence of very high metal abundances. Such low electron temperatures are also found in photoionization models constructed for chemically inhomogeneous planetary nebulae constructed by Péquignot et al. (2002, 2003) and Tylenda (2003). In these models, highly enhanced heavy element cooling via the far-IR fine-structure lines, results in the very cold inclusions conjectured in the dual-abundance model. These authors conclude that C, N, O and Ne

abundances are enhanced by a factor of 100 or even more (by number) than solar values in the posited cold and hydrogen-poor inclusions, and their mass constitutes a few per cent of the total nebular mass. If the number density n_e in the cold inclusions were about 10 times higher than that of ambient gas, the two components could be approximately in pressure equilibrium.

1.3 Application of Integral Field Spectroscopy to ORL Problems

Integral field spectroscopy (IFS) provides a unique opportunity to study the details of the ORL emission lines in an extended planetary nebula. In a recent study, Tsamis et al. (2008), utilizing an IFU FLAMES Argus on the ESO 8.2-m VLT telescope, have investigated the spatial variations in ADFs(O^{2+}) in three Galactic PNe. Their targets included the Saturn Nebula, NGC 7009, which we studied here, and they mapped the ratio of O II $\lambda\lambda$4089, 4649 ORLs to [O III] λ4959 CEL. Significant variations with a factor of about 30 in the ADFs(O^{2+}) were found over a 11.5×7.2-$arcsec^2$ field of view of VLT FLAMES, with an angular resolution of 0.52×0.52 $arcsec^2$. At the same time, they confirmed, based on the CEL T_e-diagnostic [O III] line ratio, very small values for the classical temperature fluctuations parameter t^2 for NGC 7009 (e.g. t^2=0.00075, corresponding to about 3% temperature fluctuation across their sampling area). They constrainted the physical sizes of the cold, hydrogen-poor inclusions to be less than ∼1000 astronomical units (AU), based on undulations in the C II and O II ORL abundances.

The IFU VIRUS-P (Visible Integral-field Replicable Unit Spectrograph-Prototype; Hill et al. 2008) on the McDonald 2.7-m telescope provides the largest field of view, 112×112-$arcsec^2$, amongst currently-operating IFUs. This is large enough to cover the entire bright central regions and a large portion of the extended halo of NGC 7009. This large-field advantage, together with its high sensitivity, makes VIRUS-P a suitable instrument for the study of weak optical recombination lines in extended nebulae. Compared to FLAMES Argus, VIRUS-P delivers fully-sampled maps of a 6.5 times larger field, and hence, despite its lower angular resolution (4.1″ versus 0.52″ for FLAMES), is useful to investigate spatially resolved diagnostic ORLs. The main goal of this thesis was to investigate the ORL problem in the planetary nebula NGC 7009, and to seek the implications for dual-abundance model, by exploring plausible physical conditions in the cold and hydrogen-deficient inclusions within the nebula. In Section 2, we describe the VIRUS-P observations on 2.7-meter Harlan J. Smith telescope at the McDonald Observatory, and give the details of the data reductions and analysis in Section 3. In Section 4, we present fully-sampled 2-D VIRUS-P maps of various ORL-based abundances in NGC 7009. We discuss the implications of this study for the dual-abundance model in Section 5, followed by the summary in Section 6.

Chapter 2

Observations

2.1 Properties of NGC 7009

We selected the bright planetary nebula NGC 7009 (PNG 037.7-34.5; Acker et al. 1992) which is well-known for its rich and strong O II optical recombination line spectrum (Aller and Kaler 1964; Liu et al. 1995; Hyung and Aller 1995a,b), as our primary target for this study. Liu et al. (1995), using long-slit spectroscopic observations of NGC 7009, found an averaged ionic abundance of $O^{2+}/H^{+} = (17.6 \pm 1.7) \times 10^{-4}$ from a large number of O II transitions among various 4f-3d, 3d-3p, 3p-3s levels, while deriving a lower abundance of $O^{2+}/H^{+} = 3.68 \times 10^{-4}$ and $O/H = 4.08 \times 10^{-4}$ from CELs, compared to the recent solar value of $O/H = 4.90 \times 10^{-4}$ (Allende Prieto, Lambert, and Asplund 2001). With integral field spectroscopy of the central inner shell of NGC 7009, Tsamis et al. (2008) found the same trend of higher ORL and lower CEL abundances: an average value $O^{2+}/H^{+} = (24.5 \pm 2.8) \times 10^{-4}$ from O II $\lambda\lambda$4089, 4649 and $O^{2+}/H^{+} = (3.54 \pm 0.03) \times 10^{-4}$ from [O III] λ4959 respectively. The corresponding ADFs are $\sim$5 (Liu et al. 1995) and $\sim$7 (Tsamis et al. 2008). The differences in ADFs derived above might be caused by different field sizes and/or sample regions within the nebula, implying possibly large point-to-point deviations in ADFs.

NGC 7009 is classified as an oxygen-rich PN. Values for C/O reported in the literature include C/O=0.48 or 0.37 (from ORLs and CELs respectively; Liu et al. 1995), and 0.81 (from UV and optical forbidden lines; Kwitter and Henry 1998). The optical angular diameter of the central bright region is approximately $\sim 28''.5$ (Acker et al. 1992), while the tenuous giant halo has a diameter of 216 arcsec when measured in an [O III] narrow-band filter (Moreno-Corral et al. 1998). In the context of the abundance discrepancies, the large angular extent and high surface brightness of NGC 7009 make it an optimal target for investigating spatial variations in the weak O II recombination emission, with VIRUS-P.

2.2 VIRUS-P Observations

We carried out spatially-resolved spectroscopic observations of the Saturn Nebula NGC 7009 ($\alpha_{2000} = 21^h04^m10^s.89$, $\delta_{2000} = -11°21'48''.3$) on September 14, 2007 (UT) under photometric conditions, utilizing the visible integral-field replicable unit spectrograph prototype (VIRUS-P; Hill et al. 2008) on the 2.7-m Harlan J. Smith telescope at the McDonald Observatory. VIRUS-P is an integral field unit (IFU) spectrograph consisting of 247 close-pack fibers in a hexagonal pattern. Mounted on the f/8.8 bent Cassegrain focus, VIRUS-P has an effective focal ratio of f/3.65 when used with a focal reducer. This configuration yields a spatial resolution of 4.1 arcsec per 200 μm-diameter fiber, and a 112×112- $arcsec^2$ field of view. VIRUS-P, used on the McDonald 2.7-m, delivers simultaneous spectra in 241 working fibers (ex-

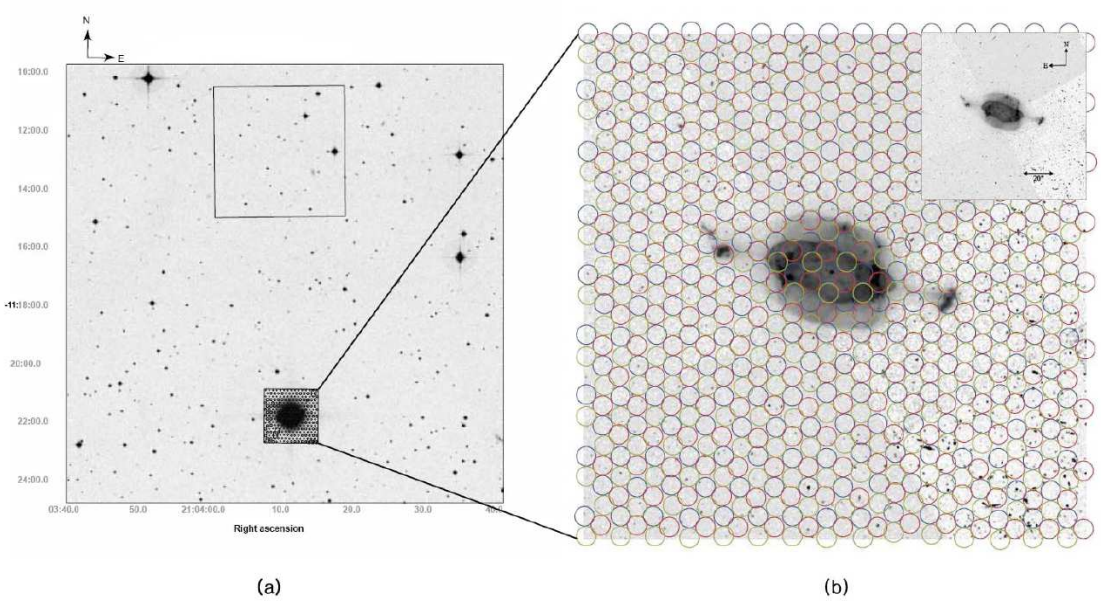

Figure 2.1 (a) The total field, and (b) the target field of VIRUS-P observations overlaid on the Hubble Space Telescope image of NGC 7009. In (a), the target field of NGC 7009 appears as the small square in the south and the larger square in the north shows the guider field. In (b), the target field of NGC 7009 is superposed with a configuration map of the 247×3 VIRUS-P fibers, and three colors, coordinated with three dithers for full spatial coverage (dither 1 in blue, dither 2 in red, and dither 3 in green). The inset shows the angular size and the position angle of field of view (credit: HST image: Bruce Balick).

cluding 6 dead fibers) over the wavelength range 3550-5850 $\AA$ at a spectral resolving power of $R(= \lambda/\Delta\lambda)$ ≈1000 at 5000$\AA$ (i.e. full width at half maximum (FWHM) of ∼5.0 $\AA$). This wavelength range covers most of the major optical O II recombination lines, in addition to a number of key H and He recombination lines and important CELs.

The total field of the VIRUS-P observation of NGC 7009, superposed on the STScI Digitized Sky Survey image, is shown in Fig. 2.1 (a), where the

Date (UT)	Wavelength (Å)	Seeing (arcsec)	Dither	Exposure (second)
Sept 14, 2007	3550-5850	∼1.0	1,2,3	1200×3 (long) 60×3 (short)

Table 2.1 A summary of the VIRUS-P observations of NGC 7009.

target field of NGC 7009 and a fixed, offset guider field containing guider stars are represented by the small square region to the south and the large square to the north, respectively. Guide stars are used to make astrometric calibrations of the fiber positions to an accuracy of $\pm 1''.0$. During these observations, the seeing was $\sim 1''.0$, significantly smaller than the angular resolution of $4''.1$. Fig. 2.1 (b) shows the target field, with a configuration map of the 247 fibers, overlaid on the Hubble Space Telescope WFPC2 image of NGC 7009. The field of view was 112×112-$arcsec^2$, and the physical scale of each $4''.1$ angular diameter fiber corresponds to 0.017 pc (or ∼3500 AU) for the distance of NGC 7009, approximately 860 pc (Fernández et al. 2004). Since VIRUS-P has a ∼1/3 filling factor, we used three offset positions (referred to as "dithers") to achieve full spatial coverage (Fig. 2.1 (b)).

Three exposures were taken for each dither position with an exposure time of 1200 seconds per frame, along with shorter exposures of 60 seconds, to try to avoid saturation in the bright lines (Table 2.1). However, some emission lines, including Hβ and [O III] λ4363, were still saturated in some of the central fibers even in the short exposures. To estimate Hβ fluxes for the saturated fibers, we measured the fluxes of the unsaturated Hγ line, and calculated the corresponding Hβ fluxes, assuming the Hγ/Hβ line ratio of 4.69×10^{-1} for

T_e=10,000K and n_e=4,500cm^{-3} in case B approximation (Storey and Hummer 1995). For the fibers where [O III] λ4363 was saturated in the long exposure, we measured both F([O III] λ4363) and F(C II λ4267) in the short exposure (both of them unsaturated), along with F(C II λ4267) in the long exposure. We used C II λ4267 to "bridge" between the long and short exposures because this line is bright (and thus well-measured), yet remained unsaturated in both long and short exposures over all of the fibers. Together with the science frames, a complete set of calibrations including bias, Hg-Cd comparisons, twilight flats, sky backgrounds, and spectrophotometric standards, were also acquired. Two spectrophotometric white dwarf stars, Feige 110 and BD+25D 4655 (Bohlin 1996), provided the flux calibration, and we nodded the telescope to north and south by 10 arcmin from the target field of NGC 7009 between the dithers in order to obtain separate sky background images. This required extra observing time, but is of crucial importance to secure proper sky subtraction for such an extended source. We binned by 2×1 in the dispersion direction in order to increase the signal-to-noise (S/N) ratio, at the sacrifice of spectral resolution. High S/N is especially important in this study, since most of the O II ORLs are very weak.

Chapter 3

Data Reduction and Analysis

3.1 Basic Reduction and Calibration

We reduced the VIRUS-P spectra according to standard CCD data reduction procedures. All the reductions were carried out with custom software written at the University of Texas and optimized for VIRUS-P multi-fiber spectra. Notably, this software does not perform resampling or modulation of the data. First, a master bias frame was created and the raw images were bias-subtracted, followed by application of a bad pixel mask. A master flat and a master arc lamp were created by combining twilight flats and Hg-Cd comparisons respectively. We then rectified the curvature in the VIRUS-P spectra, by fitting 4th-order polynomials along each fiber. The wavelength calibration was made from 12 arc lamp lines of Hg and Cd; wavelength residuals were less than $\sigma_\lambda \leq 0.3\mathring{A}$ in all 241 working fibers. Twilight flats were used to remove pixel-to-pixel variations, fiber-to-fiber variations, and the fiber illumination profile. Sky background was estimated from night sky images in separate northern and southern fields, obtained by nodding the telescope north and south by 10 arcmin from the target field between the dithers. Taking the exposure time and the time sequences of exposures into consideration, we have scaled the night sky images appropriately for each science frame. This

procedure enabled us to achieve excellent sky subtraction, with fluctuations of less than 1 % in time. Two spectrophotometric standards, Feige 110 and BD+25D 4655 (Bohlin 1996), were used for flux calibration. Three exposures of each dither were combined using a median filter, which also removed cosmic rays. For the interstellar reddening correction, we adopted the extinction value $c(\mathrm{H}\beta)$=0.20 (Liu et al. 1995), with the interstellar extinction curves of Nandy et al. (1975) and Seaton (1979). For our analysis, we masked the central fiber including the central star of the planetary nebula (CSPN). Apart from this mask, we detected O II optical recombination lines in 41 different VIRUS-P fiber positions, an approximately 6.5 times larger angular area than the previous IFU FLAMES Argus observations by Tsamis et al. (2008). In the following we give further details of our analysis of the nebular recombination emission lines measured with VIRUS-P.

3.2 Subtraction of Nebular Continuum Emission

We calculated the nebular gaseous continuum emission and subtracted it from the dereddened VIRUS-P spectra, in order to make more robust flux measurements of the weak ORLs, which have relatively low contrast to the underlying continuum, especially at the low spectral resolution of our VIRUS-P data. We used the fitting formula for nebular continuum emission from Zhang and Kwok (1991) and calculated the continuum emission individually for each fiber. The tables in Brown and Mathews (1970) were adopted to obtain the effective emission coefficient, which include free-free and bound-

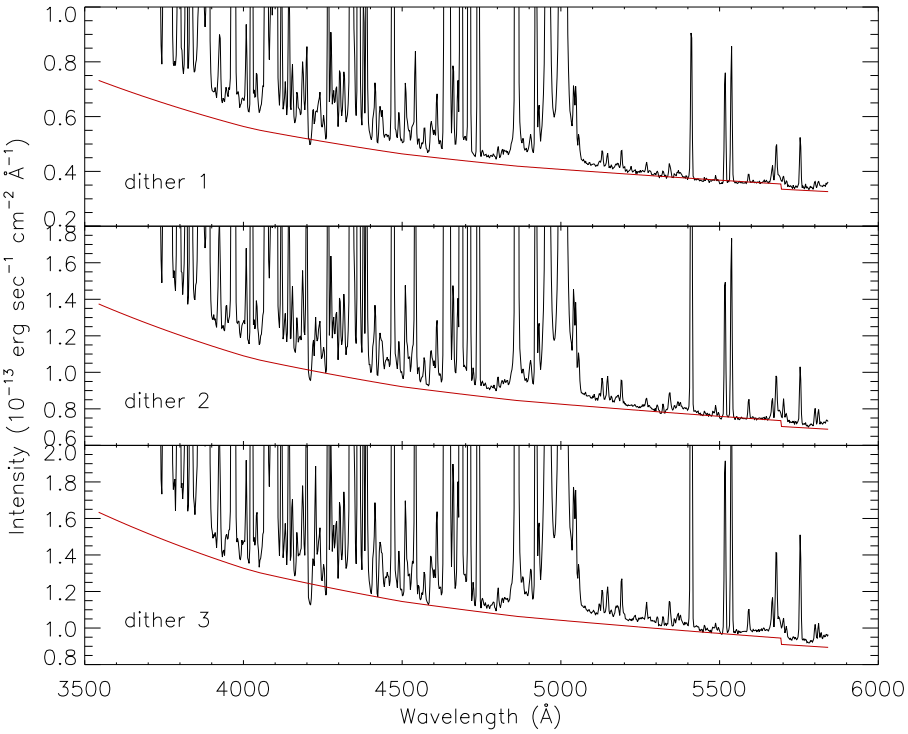

Figure 3.1 VIRUS-P spectra of NGC 7009 and the calculation of nebular gaseous continuum emission flux. The de-reddened intensity (in black) is overplotted with the calculated nebular continuum emission flux (in red). The calculated continuum was fit to fiducial, emission-line-free chunks in the spectra: $\lambda\lambda$ 4760-4820, 5210-5290, 5420-5440, 5550-5570, 5600-5650, and 5720-5740. Each panel (from top to bottom) corresponds to the fiber ID number 109 of dither 1, dither 2, and dither 3, respectively (also corresponding to unique VIRUS-P positions 8, 1, and 2 in Fig. 4.2 (a)).

free emission of H I, He I, He II, and the two-photon decay of the 2 $^2S_{1/2}$ level of H I. The resultant continuum is free of dependence on density structures (i.e. the product of $n_e n_p$), and we assumed an electron temperature of T_e=10,000 K, based on earlier references on NGC 7009 (Liu et al. 1995, Rubin et al. 2002, Tsamis et al. 2008). We scaled the continuum to fit several emission-line-free, fiducial chunks in our spectra, selected from high-spectral-resolution spectra for high- and low-excitation regions of NGC 7009 (Hyung and Aller 1995a,b). Fig. 3.1 shows an example of a fit for a representative fiber (number 109). Similar fits to all fibers were subtracted from the dereddened spectra, before measuring fluxes of emission lines.

3.3 Emission Line Measurements

The emission line measurements were performed on the continuum-subtracted and extinction-corrected spectra. We measured the intensities of selected emission lines using χ^2 minimization of Gaussian profiles. Fig. 3.2 shows an example of a multiple Gaussian fit to an important spectral region, containing the C II λ4267 and O II $\lambda\lambda$4275, 4282, 4303 recombination lines. For the line center and its vicinity, our fits were in good agreement with the data within a few per cent, while errors of about 10-15 per cent were estimated in the line wings. The latter effect might be caused by the fact that our fir procedure weighted the line centers more strongly than the wings, or, in some cases, the presence of additional weak, blending lines.

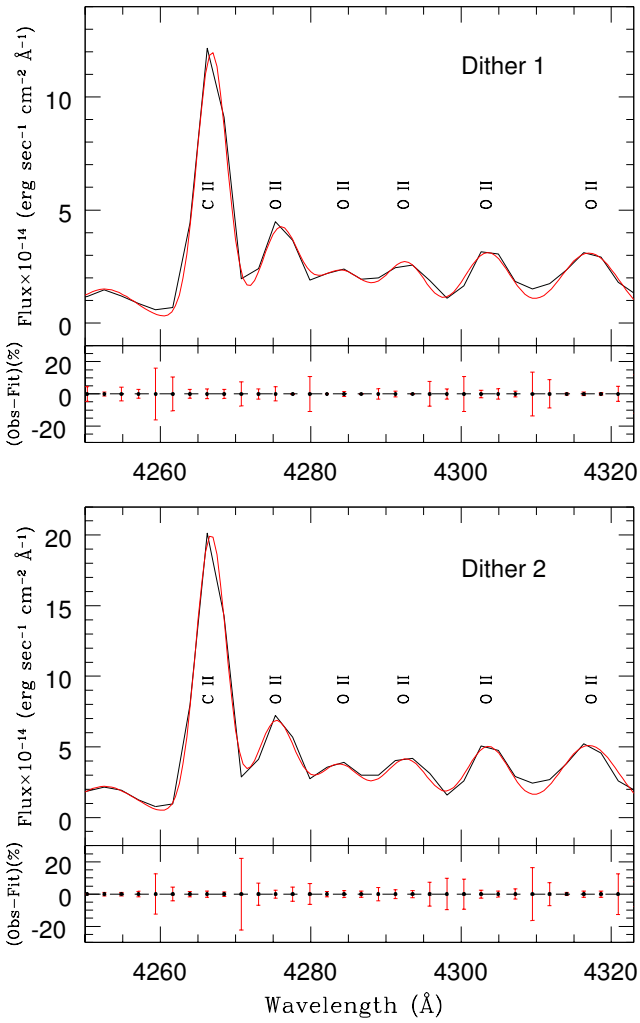

Figure 3.2 Optical recombination lines (ORLs) in VIRUS-P spectra of NGC 7009 between 4250 and 4325$\mathring{A}$. The continuum-subtracted and extinction-corrected spectra are indicated in black. The red line is the sum of a multiple Gaussian fit to the data. The Fiber number 109 of dither 1 and dither 2 are shown in the top and bottom panels respectively, together with the residual of the fit and the error bars for each data point. The 4f-3d transitions of O II $\lambda\lambda$ 4275.55, 4282.96, 4303.82 and C II λ 4267.18 ORLs, contained in this spectral segment, are favorable for ORL-based abundance determinations (refer to the text for details.).

3.4 Correction of O II ORL Fluxes for Blending

We compiled a list of the O II recombination lines in our wavelength range λ3550-5850 from previous high-spectral-resolution studies of NGC 7009 (Hyung and Aller 1995a,b; Liu et al. 1995). Many of these ORLs were detected and identified in our spectra (e.g. Fig. 3.2). However, due to the low spectral resolution of VIRUS-P, most of the lines of interest are blended to at least some extent. In the selection of specific lines for our analysis, we chose ORLs that were both relatively strong and blended only with other ORLs of O II. For the blends that meet this criterion, we defined a de-blending factor (DF) of the strongest ORL at the wavelength λ, as

$$DF(\lambda) = \frac{\alpha_{eff}(\lambda) \cdot \lambda^{-1}}{\sum \alpha_{eff}(J, J') \cdot \lambda^{-1}_{J,J'}} = \frac{(2J_\lambda + 1) \cdot B_\lambda(J, J') \cdot \alpha_\lambda \cdot \lambda^{-1}}{\sum (2J + 1) \cdot B(J, J') \cdot \alpha \cdot \lambda^{-1}_{J,J'}} \qquad (3.1)$$

where $\alpha_{eff}(J, J')$ is the effective radiative recombination coefficient of the particular transition from $J \rightarrow J'$, $B(J, J')$ is the branching ratio, and α is a function of temperature and density (Storey 1994). Under the reasonable assumption that all of the O II ORLs originate from the same region, with similar physical conditions (e.g. T_e, n_e), the DF gives the fractional contribution of the strongest O II recombination line to the blended feature. We adopted branching ratio values $B(J, J')$ from Liu et al. (1995), which are calculated for intermediate-coupling of O II ORLs.

To determine the deblending factors of O II ORLs, we adopted an electron temperature of T_e = 10,000K, which is a reasonable assumption, based on its tiny value of the temperature fluctuation parameters t^2_A([O III])=0.00075

(Tsamis et al. 2008), comparable to about a 3% temperature fluctuation. Notably, it is valid for the single abundance case. However, it is also very crucial to ensure that this scheme of the DF would work for the dual-abundance paradigm, wherein most ORLs originate from the cold, hydrogen-deficient inclusions, not from the ambient hot (T_e=10,000K) nebular gas. We therefore calculated the DFs for both hot and cold temperatures of T_e=10,000K and 500K respectively. The high electron temperature T_e=10,000K represents the single abundance case, while the low T_e=500K value is relevant for the dual-abundance model in which we assume that most ORLs arise from the cold inclusions. This value, T_e=500K, was taken from the recent observational evidence for very low T_e values from O II ORL line ratios (Liu et al. 2004; Tsamis et al. 2004; Wesson et al. 2005; Bastin and Storey 2006). Detailed photoionization models incorporating hydrogen-deficient inclusions have also yielded low T_e values ($\sim$1,000 K) for a few PNe; NGC 6153, M 1-42, and M 2-36 (Péquignot et al. 2002, 2003; Tylenda 2003).

We compared the predicted ratio of O II recombination lines with the observed ratios from high-spectra-resolution spectra in Hyung et al. (1995a,b) and Liu et al. (1995). In Fig. 3.3, the published dereddened intensities of the O II 4f-3d transitions at $\lambda\lambda$4083.90, 4087.16 and O II 3d-3p transitions at $\lambda\lambda$4092.93, 4085.12 are normalized to the intensity of O II λ4089.29 ORL, one of the five lines we used in our study. We compare these to the predictions for these ratios at T_e=10,000K and 500K. Overall, as shown in Fig. 3.3, the predicted line ratios are similar for both values of T_e, and also are in

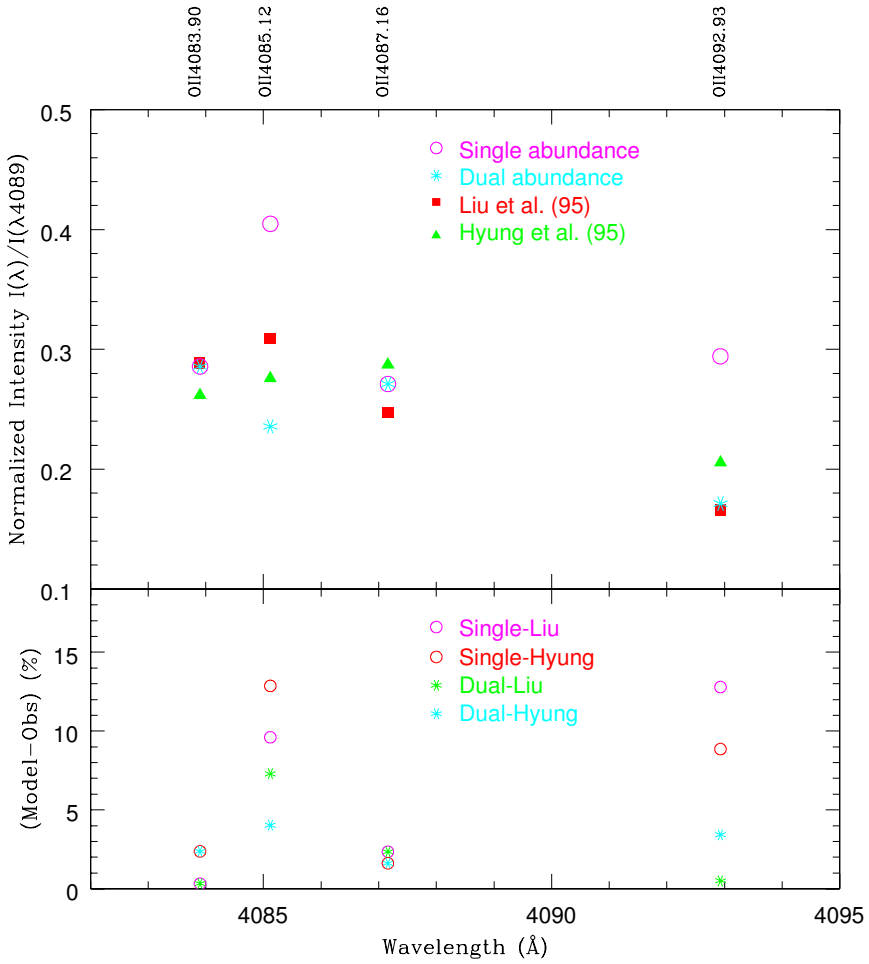

Figure 3.3 The intensity ratios of various O II ORLs to I(O II λ4089) from the models and the observations. Four O II $\lambda\lambda$4083.90, 4085.12, 4087.16, 4092.93 ORLs were examined in the vicinity of O II λ4089.29 ORL. The model-predicted ORL intensities were calculated for T_e=10,000K (Single abundance; magenta unfilled circle in the top panel), 500K (Dual abundance; cyan asterix), and the observed ORL intensities were adopted from Liu et al. (1995) (red filled rectangle) and Hyung and Aller (1995) (green filled triangle). The residuals between the model predictions and the observational measurements are compared in the bottom panel. Overall, the models are in good agreement with the observations within 15 per cent errors at most, although the dual abundance predictions (green and cyan asterix in the bottom panel) gave rise to better results than the single abundance cases (cyan and red unfilled circle).

good agreement with the observed ratios. Therefore, our computed DF values are valid for a wide range of T_e and can be applicable for both single and dual-abundance cases. The O II 4f-3d transitions, for both hot and cold temperatures, resulted in relatively better agreement with the observations, within 3 % errors, while the 3d-3p transitions showed larger differences of $\sim$5 %, $\sim$10 % for T_e=500K and 10,000K respectively (bottom panel in Fig. 3.3). This might be an interesting outcome because the lower electron temperature case (for dual-abudance model), reproduces the observed line ratios better than the high electron temperature (for single abundance) for certain O II recombination lines (in 3d-3p transition). We took the T_e=10,000K to derive the values of the DFs for the subsequent analysis of ionic abundance determinations, but the details of the dual-abundance model will also be taken into consideration, in Section 5.

Chapter 4

Results

4.1 Ionic Abundance Determinations from ORLs

The ionic abundance relative to hydrogen derived from a given ORL of the ion X^{+i} in VIRUS-P spectra is given by

$$\frac{X^{+i}}{H^+} = \frac{\varepsilon(H\beta)}{\varepsilon(\lambda)} \frac{I(\lambda)}{I(H\beta)} \times DF = \frac{\lambda(\mathring{A})}{4861} \frac{\alpha_{eff}(H\beta)}{\alpha_{eff}(\lambda)} \frac{I(\lambda)}{I(H\beta)} \times DF \qquad (4.1)$$

where $\varepsilon(\lambda)$ is the density-normalized emissivity of the recombination line at λ $\mathring{A}$ ($erg\ cm^3\ s^{-1}$), $\alpha_{eff}(\lambda)$ is the radiative effective recombination coefficient ($cm^3\ s^{-1}$), $I(\lambda)$ is the measured intensity of the blends, and DF is the deblending factor for the strongest recombination line in the blends (see Section 3.4). For the calculations of the effective recombination coefficients of the O II, C II, H I, He I, and He II ORLs in this section, we have adopted T_e = 10,000 K and n_e = 4,500 cm^{-3} for NGC 7009, based on earlier papers (Liu et al. 1995, Rubin et al. 2002, Tsamis et al. 2008). Some uncertainties may be introduced by the assumption of a constant electron temperature and electron density, but the effect on the ORLs abundance determinations should be very small. The temperature dependences of α_{eff} in heavy element ORLs and H I lines are so similar that they virtually cancel, while density dependence of the α_{eff} values are rather minor over a wide range of n_e in PNe. Moreover,

as mentioned earlier, tiny value of temperature fluctuation parameter, t_A^2([O III])=0.00075, in NGC 7009 (Tsamis et al. 2008) justifies the assumption of a constant temperature.

The O II transitions to be used for abundance determinations have been carefully selected from those which blended only with other O II lines, not with lines from other elements or other ionization states. The branching ratios $B(J, J')$ and fitting functions for the effective recombination coefficients for the 4f-3d and 3d-3p transitions of O II ORLs were obtained from Liu et al. (1995). For the 3p-3s transitions, the α_{eff} were taken from Storey (1994). The α_{eff} of the H I lines were interpolated for case B from Storey and Hummer (1995). Then the ratios of O^{2+}/H^+ ionic abundances derived from the individual O II ORLs were checked to avoid systematic bias caused by potential blends with unknown emission features. For this purpose, we compared the ratios of relative abundances determined from different O II ORLs. Fig. 4.1 shows the abundance ratios from different O II lines for the fibers in dither 3. The $\lambda\lambda$4132, 4491 lines yielded systematically higher O^{2+}/H^+ values than the other lines (the former might be contaminated by Ar II λ4128.65 and the latter by N II λ4488.15) and hence were ruled out. The ionic abundances determined from individual O II ORLs here were estimated to be accurate to 10 per cent from the averaged abundances in most positions, up to about 30 per cent in some cases. The scatter between abundances determined from different ORLs were taken to be representative of the rms errors.

We selected five O II ORLs as the best indicators for abundance deter-

Element	$\lambda(\AA)$	Transition	Branching Ratio	Deblending Factor	Effec. Recom. Coefficient
O II	4089.29	4f $G[5]_{11/2}$-3d $^4F_{9/2}$	1.000	0.434	(a)
O II	4275.55	4f $F[4]_{9/2}$-3d $^4D_{7/2}$	0.681	0.427	(a)
O II	4282.96	4f $F[2]_{5/2}$-3d $^4D_{3/2}$	0.323	0.240	(a)
O II	4303.82	4f $D[3]_{7/2}$-3d $^4P_{5/2}$	0.652	0.591	(a)
O II	4676.24	3p $^4D_{5/2}$-3s $^4P_{5/2}$	-	0.794	(b)
C II	4267.18	4f $^2F^o$-3d $^2D^e$	-	1.0	(c)
He I	4471.44	4d ^3D-2p $^3P^o$	-	1.0	(d)
He II	4685.71	4-3	-	1.0	(e)
H I	4861.33	4-2	-	1.0	(e)
[O II]	3726.03	$^4S^0_{3/2}$-$^2D^0_{3/2}$	-	1.0	(f)†
[O II]	3728.82	$^4S^0_{3/2}$-$^2D^0_{5/2}$	-	1.0	(f)†
[O III]	4363.21	$^1S_0$-$^1D_2$	-	1.0	(f)†

Table 4.1 A list of diagnostic emission lines in VIRUS-P spectra. Five O II optical recombination lines (ORLs) listed above were used to derive an averaged ionic ORL abundances. The forbidden lines [O III] λ4363 and [O II] $\lambda\lambda$3726,3729 were used to determine the collisionally excited line (CEL) ionic abundances. The C^{2+}/H^+ ORL abundance was derived from C II λ4267 which has also played a role of "bridging" between long and short exposures for saturated lines. The helium abundances He^+/H^+, He^{2+}/H^+ were obtained from He I λ4471 and λ4686 respectively.

References

(a): Liu, X.-W., Storey, P. J., Barlow, M. J. Clegg, R. E. S. 1995, MNRAS, 272, 369
(b): Storey, P. J. 1994, A&A, 282, 999
(c): Davey, A. R., Storey, P. J., Kisielius, R. 2000, AAS, 142, 85
(d): Smits, D. P. 1996, MNRAS, 278, 683
(e): Storey, P. J., and Hummer, D. G. 1995, MNRAS, 272, 41
(f): Shaw, R. A., and Dufour, R. J. 1994, ASPC, 61, 327 (5-level atom program)
†: Volume emissivity, not the effective recombination coefficient

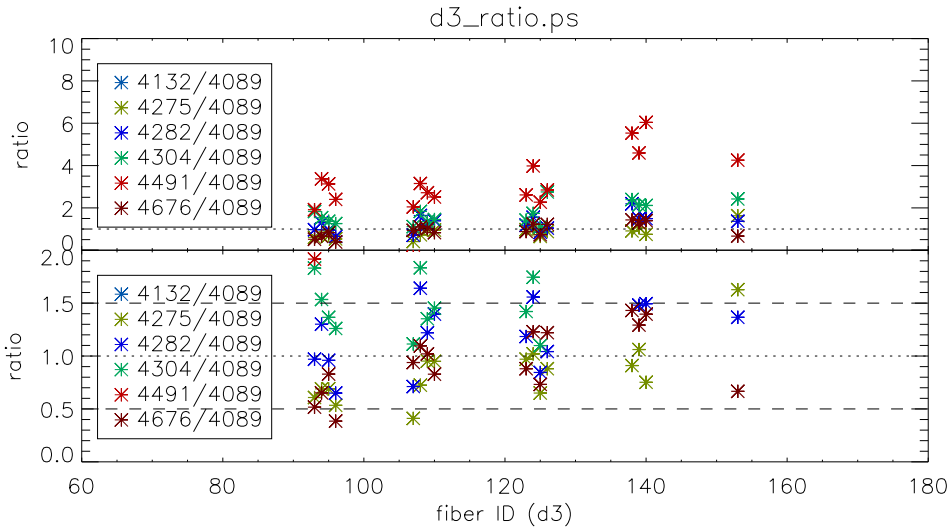

Figure 4.1 The ratios of O^{2+}/H^{+} ionic abundances derived from different O II ORLs, for 21 fibers in dither 3. Note the change in scale from the top to bottom panels. This comparison allowed us to check for systematic bias in the derived abundances. The $\lambda\lambda$4132, 4491 lines yielded systematically higher abundances and thus were eliminated.

minations, based on the following criteria: i.e. (a) a pure blend of O II ORLs, (b) no systematic bias shown in derived abundances, (c) an accuracy within a maximum deviation of about 30 per cent. Table 4.1 lists the transitions of the selected O II ORLs; four 4f-3d transitions, $\lambda\lambda$ 4089, 4275, 4282, 4303, and a 3p-3s transition, λ 4676. The 4f-3d transitions are particularly reliable as ORL abundance indicators because they are insensitive to the optical depth (hence independent of case) and are free of fluorescence enhancement (Liu et al. 2003). Although LS-coupling breaks down for these transitions, O II ORL λ4089, the strongest line in this group, is immune to the coupling scheme (i.e. $B(J, J') = 1.0$; Liu et al. 1995). O II λ4676, a 3p-3s transition in multiplet 1 (M 1), is blended with another O II line, M 1 λ4674, in our VIRUS-P spectra, and thus a correction was made for this. In general, O II λ4676 has been considered to be reliable data, but suffered from somewhat inaccurate flux calibrations because it lies on the wing of the very strong He II λ4686 line.

Abundance	VIRUS-P[(a)]	VIRUS-P (PA=0°)	Liu 95[(b)] (PA=0°)	Tsamis 08[(c)]
O^{2+}/H^+ ORL ($\times 10^{-3}$)[(d)]	2.43±0.19	2.70±0.49	2.12±0.47	3.12±0.25[(e)]
C^{2+}/H^+ ORL ($\times 10^{-4}$)[(f)]	5.88±0.43	7.54±0.11	7.38	10.10±0.50
He^+/H^+ ORL ($\times 10^{-1}$)[(g)]	1.04±0.06	1.03±0.07	0.90[(h)]	0.95±0.04
He^{2+}/H^+ ORL ($\times 10^{-2}$)[(i)]	0.61±0.03	1.45±0.10	1.49	2.13±0.03
O^+/H^+ CEL ($\times 10^{-5}$)[(j)]	1.16±0.05	0.74±0.01†	0.50†	-
O^{2+}/H^+ CEL ($\times 10^{-4}$)[(k)]	4.79±0.20	3.85±0.27†	3.53[(l)]†	3.54±0.03[(m)]
ADF(O^{2+})[(n)]	5.34±0.41	7.02±1.37	6.02	9.10±0.74[(o)]

Table 4.2 A summary of VIRUS-P ionic abundance determinations and the abundance discrepancy factor (ADF). The abundances from the simulated long-slit spectrum based on VIRUS-P data at position angle (PA) = 0° (third column) were compared with those from the long-slit spectra in Liu et al. (1995) of the same PA (fourth column). The results from VLT FLAMES (Tsamis et al. 2008) are also listed here for the comparison.

(a): Mean values for all 41 positions that satisfy the selection criteria (Section 4.1). The CEL abundances and ADFs were averaged over 34 positions (see the Section 4.5 for more details.).
(b): Liu, X.-W., Storey, P. J., Barlow, M. J. Clegg, R. E. S. 1995, MNRAS, 272, 369 (for NGC 7009)
(c): Tsamis, Y. G., Walsh, J. R., Péquignot, D., Barlow, M. J., Danziger, I. J., Liu, X.-W. 2008, MNRAS, 386, 22
(d): O^{2+}/H^+ is the averaged value for the five O II ORLs listed in Table 4.1.
(e): based on O II λ4089 ORL
(f): based on C II λ4267 ORL
(g): based on He I λ4471 ORL
(h): based on He I $\lambda\lambda$4471, 5876 and 6678 ORLs
(i): based on He II λ4686 ORL
(j): based on [O II] $\lambda\lambda$3726+3729 CELs
†: based on T_e=10,180K (Liu et al. 1995)
(k): based on [O III] λ4363 CEL
(l): based on [O III] $\lambda\lambda$4959,5007 CELs
(m): based on [O III] λ4959 CEL
(n): ADF(O^{2+}) = $(O^{2+}/H^+)_{ORL}/(O^{2+}/H^+)_{CEL}$
(o): based on O II λ4089 ORL and [O III] λ4959 CEL

Table 4.3. VIRUS-P fibers with O II ORL abundances in NGC 7009

Position ID†	R.A. (J2000)	Dec. (J2000)	I($H\beta$) ($\times10^{-11}$)	O^{2+}/H^+ ORL ($\times10^{-3}$)	C^{2+}/H^+ ORL ($\times10^{-4}$)	He^+/H^+	He^{2+}/H^+ ($\times10^{-2}$)	O^{2+}/H^+ CEL ($\times10^{-4}$)	ADF(O^{2+})	Mass Fraction‡ ($\times10^{-2}$)
1	21:4:10.88	-11:21:43.1	12.468±0.087	3.103±0.782	8.253±0.168	0.103±0.005	1.683±0.077	3.527±0.154	8.797±2.251	5.483±1.431
2	21:4:11.13	-11:21:45.2	14.529±0.269	2.975±0.456	8.698±0.181	0.094±0.004	1.704±0.072	3.350±0.143	8.879±1.413	4.525±0.742
3	21:4:11.14	-11:21:49.7	15.547±0.116	4.513±0.500	11.494±0.492	0.103±0.006	2.092±0.130	3.829±0.233	11.785±1.490	11.014±3.715
4	21:4:10.87	-11:21:51.9	13.363±0.100	3.062±0.359	8.880±0.274	0.095±0.015	2.044±0.312	3.585±0.548	8.542±1.644	5.738±1.600
5	21:4:10.62	-11:21:49.8	15.348±0.197	2.881±0.574	8.139±0.351	0.107±0.006	1.627±0.094	3.461±0.197	8.326±1.724	4.499±0.877
6	21:4:10.60	-11:21:45.2	13.576±0.229	3.730±0.929	10.969±0.322	0.114±0.006	1.170±0.060	3.547±0.183	10.516±2.675	6.123±1.278
7	21:4:10.87	-11:21:38.6	3.102±0.093	1.462±0.382	3.891±0.203	0.114±0.004	0.110±0.006	4.360±0.135	3.353±0.881	1.939±0.706
8	21:4:11.14	-11:21:41.0	7.103±0.034	2.757±0.463	8.788±0.125	0.106±0.001	0.642±0.015	4.254±0.041	6.482±1.090	6.322±1.934
9	21:4:11.39	-11:21:43.1	8.296±0.187	2.514±0.505	6.930±0.257	0.105±0.003	0.709±0.046	4.592±0.302	5.474±1.157	3.769±0.832
10	21:4:11.40	-11:21:47.6	11.717±0.081	2.338±0.523	6.356±0.173	0.096±0.004	0.793±0.030	3.986±0.159	5.866±1.333	3.546±0.823
11	21:4:11.39	-11:21:51.8	11.275±0.249	2.688±0.530	8.184±0.256	0.103±0.007	0.699±0.047	4.756±0.291	5.652±1.167	4.154±0.758
12	21:4:11.15	-11:21:54.3	9.671±0.085	2.333±0.339	7.028±0.356	0.102±0.002	1.254±0.089	4.006±0.280	5.824±0.940	3.588±0.899
13	21:4:10.89	-11:21:56.4	9.452±0.126	2.275±0.423	6.671±0.157	0.096±0.002	0.953±0.037	4.278±0.075	5.318±0.993	3.703±1.115
14	21:4:10.62	-11:21:54.2	15.662±0.085	2.625±0.569	8.398±0.162	0.103±0.003	1.061±0.029	4.528±0.118	5.796±1.266	4.036±0.838
15	21:4:10.35	-11:21:51.8	9.805±0.129	2.023±0.433	5.313±0.265	0.114±0.003	0.602±0.045	5.109±0.391	3.960±0.900	2.961±0.879
16	21:4:10.36	-11:21:47.6	12.291±0.119	3.661±1.133	8.985±0.358	0.119±0.007	0.471±0.033	4.937±0.293	7.415±2.337	6.238±1.446
17	21:4:10.35	-11:21:43.1	4.145±0.070	1.895±0.447	4.831±0.180	0.112±0.003	0.150±0.011	4.436±0.100	4.273±1.013	2.579±0.855
18	21:4:10.61	-11:21:41.0	6.118±0.041	2.416±0.795	4.664±0.114	0.114±0.001	0.155±0.004	3.704±0.040	6.523±2.147	3.760±1.256
19	21:4:10.88	-11:21:34.4	0.197±0.005	4.210±0.423	7.678±0.573	0.126±0.005	0.339±0.013	9.359±0.279	4.499±0.472	10.947±4.701
20	21:4:11.13	-11:21:36.3	0.890±0.013	2.590±0.670	5.787±0.351	0.120±0.005	0.177±0.010	6.291±0.151	4.118±1.070	6.077±2.715
21	21:4:11.38	-11:21:38.4	1.499±0.077	2.405±0.801	5.104±0.444	0.113±0.006	0.152±0.011	5.502±0.290	4.371±1.475	4.446±1.556
22	21:4:11.65	-11:21:41.0	2.042±0.023	2.130±0.725	4.454±0.316	0.097±0.004	0.532±0.019	5.076±0.153	4.197±1.434	3.663±1.493
23	21:4:11.64	-11:21:45.2	5.964±0.058	1.769±0.363	4.600±0.131	0.105±0.002	0.731±0.036	5.400±0.087	3.277±0.675	3.501±1.563
24	21:4:11.65	-11:21:49.7	5.367±0.165	1.849±0.374	5.302±0.448	0.098±0.004	0.483±0.020	5.073±0.214	3.644±0.753	3.483±1.490
25	21:4:11.66	-11:21:54.3	1.820±0.014	1.186±0.436	2.470±0.310	0.086±0.003	0.155±0.009	4.241±0.175	2.798±1.034	1.379±0.736
26	21:4:11.40	-11:21:56.4	3.342±0.084	1.049±0.348	2.966±0.247	0.104±0.004	0.168±0.010	4.344±0.137	2.414±0.804	0.996±0.585
27	21:4:11.14	-11:21:58.5	4.019±0.069	1.341±0.335	3.540±0.164	0.102±0.002	0.137±0.009	4.276±0.079	3.136±0.786	2.648±1.493
28	21:4:10.90	-11:22:00.8	1.480±0.011	0.877±0.262	2.944±0.077	0.100±0.002	0.153±0.003	4.920±0.106	1.782±0.533	1.278±0.926
29	21:4:10.61	-11:21:58.4	3.475±0.101	1.823±0.333	5.162±0.261	0.100±0.003	0.197±0.010	4.493±0.139	4.058±0.752	2.973±1.230
30	21:4:10.36	-11:21:56.3	4.890±0.114	1.803±0.448	4.677±0.292	0.103±0.003	0.415±0.016	5.219±0.145	3.455±0.865	3.115±1.455
31	21:4:10.12	-11:21:54.3	3.614±0.052	1.935±0.482	4.564±0.265	0.105±0.003	0.525±0.018	5.564±0.162	3.478±0.872	2.679±0.902
32	21:4:10.10	-11:21:49.7	4.577±0.138	1.634±0.305	4.977±0.347	0.103±0.005	0.487±0.018	5.611±0.208	2.913±0.553	2.423±0.798
33	21:4:10.03	-11:21:44.2	0.818±0.057	2.297±0.439	4.409±0.602	0.110±0.009	0.191±0.014	6.365±0.469	3.609±0.739	4.278±2.019
34	21:4:10.35	-11:21:38.6	0.499±0.090	4.922±1.897	4.876±0.910	0.119±0.022	0.179±0.032	7.037±1.269	6.995±2.977	7.851±3.406
35	21:4:11.91	-11:21:43.0	0.819±0.042	2.987±0.924	6.080±0.461	0.110±0.007	0.636±0.050	-	-	4.396±1.805
36	21:4:11.91	-11:21:47.6	1.233±0.022	1.179±0.236	3.416±0.557	0.073±0.006	0.379±0.041	-	-	2.078±1.427
37	21:4:11.65	-11:21:58.5	0.476±0.041	1.751±0.505	2.691±0.478	0.091±0.009	0.197±0.019	-	-	2.758±1.407
38	21:4:10.38	-11:22:00.8	1.095±0.009	1.230±0.161	3.573±0.152	0.109±0.002	0.120±0.002	-	-	1.856±0.947
39	21:4:10.11	-11:21:58.5	0.779±0.022	1.610±0.480	3.183±0.303	0.093±0.005	0.131±0.004	-	-	2.500±1.333
40	21:4:09.84	-11:21:51.7	0.623±0.022	2.988±0.407	6.843±0.583	0.108±0.005	0.227±0.021	-	-	6.293±4.170
41	21:4:12.16	-11:21:45.1	0.443±0.005	4.729±0.851	5.256±0.198	0.101±0.003	0.197±0.011	-	-	6.386±2.921

Note. — †: The detailed positions of individual VIRUS-P fibers are uniquely numbered in Fig. 4.2 (a).
‡: The mass fractions are calculated for the model 4 in Table 5.1.

The O II ORLs chosen for abundance determinations were detected in 41 fibers, whose individual positions are numbered for identification purpose in Fig. 4.2 (a) (color-shaded fibers). We averaged the values from the five O II ORLs to derive a mean value per fiber, listed in Table 4.3. These averaged O^{2+}/H^{+} ORL abundances are displayed in Fig. 4.2 (b). The mean of the averaged abundances for all 41 fibers was $(2.43\pm0.19)\times10^{-3}$. This result is in good agreement with the value $O^{2+}/H^{+}= (2.12\pm0.47)\times10^{-3}$ for the same five O II ORLs obtained in a long-slit spectrum for NGC 7009 (position angle=0°) by Liu et al. (1995) (Table 4.2). Tsamis et al. (2008) obtained $O^{2+}/H^{+}=(3.12\pm0.25)\times10^{-3}$ (measured from O II λ4089 alone) for a smaller, central region of NGC 7009. Our result, $O^{2+}/H^{+}=(3.08\pm0.39)\times10^{-3}$ when measured with the same line for the same central region, is in excellent agreement with the result by Tsamis et al. (2008).

We also detected the 4f-3d transition (multiplet 6) of C II at λ4267.18 in all 41 positions (Table 4.1). This line is by far the strongest C II recombination line in the visible wavelength region and, like O II λ4089, its strength does not depend on optical depth or coupling scheme. Its spectral isolation in wavelength space is especially beneficial in low spectral-resolution data, such as VIRUS-P. As described in Section 2.2, C II λ4267 also played an essential role in "bridging" between long and short exposures for the saturated lines in VIRUS-P spectra (e.g. Hβ, He I λ4471, He II λ4686, [O III] λ4363 and [O II] λ3726+3729 CELs). We adopted the effective recombination coefficient of C II ORL λ4267.18 from Davey et al. (2000), for T_e = 10,000 K. The mean C

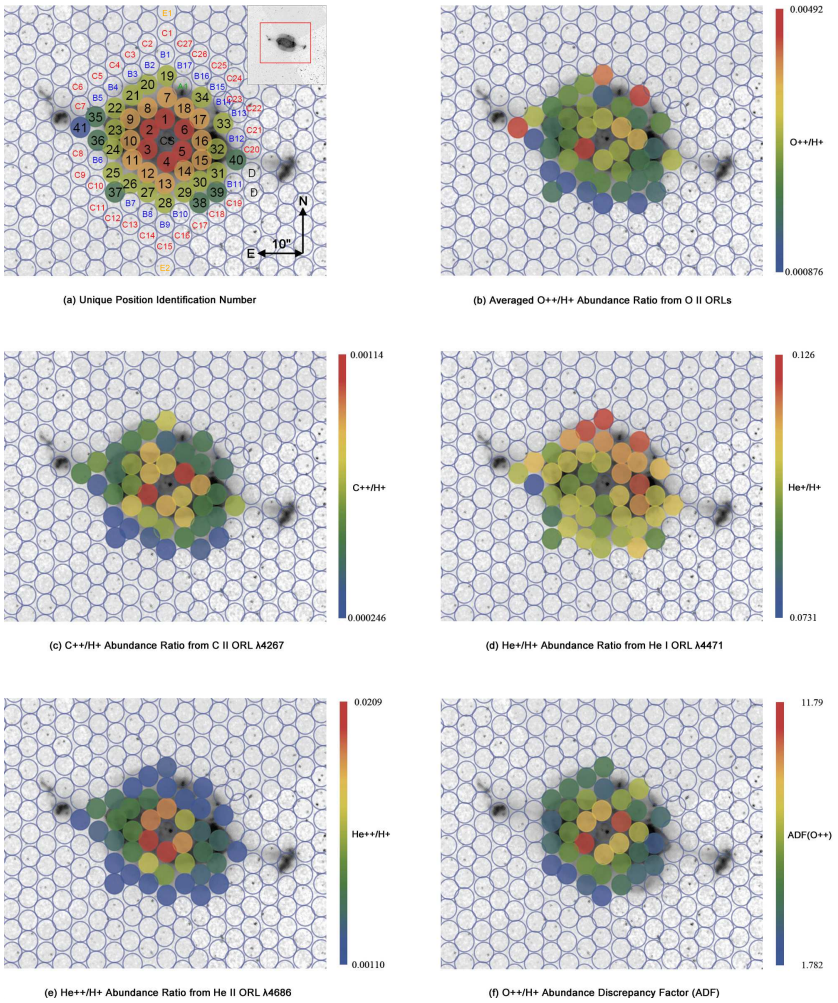

(a) Unique Position Identification Number

(b) Averaged O++/H+ Abundance Ratio from O II ORLs

(c) C++/H+ Abundance Ratio from C II ORL λ4267

(d) He+/H+ Abundance Ratio from He I ORL λ4471

(e) He++/H+ Abundance Ratio from He II ORL λ4686

(f) O++/H+ Abundance Discrepancy Factor (ADF)

Figure 4.2 VIRUS-P maps of the ORL-based abundances and the abundance discrepancy factors (ADFs) in NGC 7009. In Fig. (a), the individual VIRUS-P fiber positions were numbered for identification, and also colored to show the radial binning pattern (i.e. the concentric contour binning groups in Table 4.4. The inset in (a) shows the entire VIRUS-P target field (same as (b) in Fig. 2.1), and the red rectangle corresponds to the magnified area of NGC 7009 presented in (b)-(f). The O^{2+}/H^{+}, C^{2+}/H^{+}, He^{+}/H^{+}, He^{2+}/H^{+} ORL abundances are shown for 41 VIRUS-P positions, from (b) to (e) respectively. The ADF values for 34 VIRUS-P positions within the radius of 14 arcsec are shown in (f), where the gradient in T_e for the hot gas was taken into account in determining the CEL abundances (see Section 4.5 for details.).

II ORL abundances for the 41 fibers were C^{2+}/H^{+}=(5.88±0.43)×10^{-4} with an rms scatter of 2.26×10^{-4}, indicating wide spread in C II ORL abundances within the measured area. Fig. 4.2 (c) shows the 2-D spatial distribution of C II ORL abundances in NGC 7009, and the abundances for the individual fibers are listed in Table 4.3. The comparison with earlier results by Liu et al (1995) and Tsamis et al. (2008) was given in Table 4.2, and are also discussed in Section 4.2.

The He^{+}/H^{+}, He^{2+}/H^{+} ionic abundances were derived from He I λ4471 and He II λ4686 relative to Hβ, respectively (Table 4.3). The effective recombination coefficients for He I λ4471, He II λ4686 were taken from Smits (1996) and Storey and Hummer (1995) respectively (Table 4.1). We obtained mean values of He^{+}/H^{+}=(1.04±0.06)×10^{-1}, $He^{2+}/H^{+} = (0.61 \pm 0.03) \times 10^{-2}$ for the 41 fiber positions (Table 4.2), and the corresponding 2-D maps are presented in Fig. 4.2 (d) and (e).

4.2 Comparison with Long-Slit Spectra of Liu et al. (1995)

We now compare the abundance determinations from our VIRUS-P spectroscopy with those from the long-slit data at higher spectral resolution, FWHM∼1$\mathring{A}$, of Liu et al. (1995). As discussed earlier, careful analysis is required for abundance determinations from the ORLs, due to their weakness (typically 0.1-0.01% of Hβ flux) and relatively small line-to-continuum ratios. Since determination of the underlying continuum level is less problematic at

higher spectral resolution, this comparison helps us test the validity of our procedures.

We simulated the long-slit aperture of Liu et al. (1995) by summing the individual VIRUS-P fibers matching the long-slit configuration. The details of our binning patterns can be found in Table 4.4. For the present comparison, we selected the position angle (PA) = 0° observation in Liu et al. (1995), which delivers the best-matching exposure time and slit width with VIRUS-P spectra, and was taken with a CCD rather than the IPCS (Image Photon Counting System). The slit width and length in this long-slit spectrum was ∼2.0-arcsec×4.5-arcmin (Liu et al. 1995), about half the width of each VIRUS-P fiber and about twice as long as the entire VIRUS-P field of view (FOV) respectively. Some minor uncertainties might be introduced by the loss of incoming light from the outer part beyond the VIRUS-P FOV in the simulated long slit, but the comparison should be still reasonable for our purpose because most of the ORLs were detected only in the central regions, within a 20-arcsec radius. Since the PA=0° long-slit spectrum in Liu et al. (1995) used masking of the central 4″, we excluded the central fiber overlaid on the central star (denoted as "CS" in Fig. 4.2 (a)). We then processed and analysed the simulated long-slit data in the same manner as performed for each fiber.

Table 4.4. Binning of VIRUS-P spectra

Binning Scheme[a]	Binning Group[b]	Binning Fiber[c]	O^{2+}/H^+ ORL ($\times 10^{-3}$)	C^{2+}/H^+ ORL ($\times 10^{-4}$)	ADF(O^{2+})
Radius (Concentric Contour)	Group 1	(1-6)	3.51±1.12	9.25±0.12	7.97±2.54
	Group 2	(7-18)	2.35±0.60	7.10±0.07	5.95±1.53
	Group 3	(19-34, A1)	1.78±0.49	4.39±0.082	5.04±1.39
	Group 4	(35-40, B1-B17)	3.08±1.20	4.62±0.147	6.94±2.70
	Group 5	(41, C1-C27)	4.38±1.67	4.79±0.32	6.27±2.40
I(Hβ)	Group 1	(3, 5, 14)	3.30±0.59	8.89±0.20	7.60±1.39
	Group 2	(2, 4, 6)	3.04±0.67	9.29±0.14	6.87±1.55
	Group 3	(1, 10, 11, 16)	2.75±0.84	7.80±0.13	6.75±2.06
	Group 4	(9, 12, 13, 15)	2.34±0.58	6.81±0.14	5.87±1.47
	Group 5	(8, 18, 23, 24)	2.61±0.80	5.95±0.11	7.15±2.20
	Group 6	(7, 17, 26, 27, 29, 30, 31, 32)	1.81±0.50	4.51±0.09	5.16±1.47
	Group 7	(19, 20, 21, 22, 25, 28, 33, 34, 35, 36, 37, 38, 39, 40, 41)	1.98±0.60	3.89±0.11	5.38±1.66
Long Slit (Liu 95, PA=0°)	Group 1	(1, 4, 7, 13, 19, 28, B1, B9, C1, C15, E1, E2 + 13 more[d])	2.70±0.49	7.54±0.11	7.02±1.37

Note. — (a) Three binning schemes have been used; (i) binning by radius, where we added up the individual fibers along concentric contours centered on the CSPN, (ii) binning by I(Hβ), where we binned fibers at similar Hβ intensities with a bin size of $\triangle$I(Hβ)=2.5$\times 10^{-11}$ $erg\ sec^{-1}\ cm^{-2}\ \mathring{A}^{-1}$, (iii) a simulated long-slit, matching the data of Liu et al. (1995) at PA=0°.
(b) (i) Radius: Group 1 (innermost contour) to Group 5 (outmost contour), (ii) I(Hβ): Group 1 (brightest) to Group 7 (faintest)
(c) The fiber ID's in this column are identical to the VIRUS-P fiber ID number in Table 4.3. Detailed positions can be found in Fig. 4.2 (a).
(d) Aside from the fibers shown in this cell, extra six and seven VIRUS-P fibers were also added up for the long-slit binning along PA=0° in north and south respectively.

The results of this comparison are shown in Table 4.2. Overall the ORL abundances derived from the simulated long-slit spectrum were in good agreement with actual long-slit spectrum within the 1-σ error bars. In particular, the C^{2+}/H^{+} and He^{2+}/H^{+} ORL abundances agree within 2 %, and He^{+}/H^{+} within 10 %. The O^{2+}/H^{+} ORL abundance averaged from the five O II lines in the simulated spectrum were about 20 per cent higher than the Liu's long-slit result, which may be due to propagated uncertainties in the deblending factors of our lower resolution data (see Section 3.4 as well). On the other hand, the O^{+}/H^{+} CEL abundances differ by $\sim$35 per cent between the simulated spectrum and the fiducial data. This may be caused by uncertainties in the flux calibrations at the blue edge of the VIRUS-P data ($\lambda \leqslant 3750\mathring{A}$), due to the low sensitivity there. On the other hand, the O^{2+}/H^{+} CEL abundance determined from [O III] λ4363 forbidden line in the simulated spectrum was in good agreement with the actual long-slit data. The 9 per cent higher O^{2+}/H^{+} CEL-based abundance was obtained from the simulated spectrum compared to the Liu's long slit result, and they both match well within 1-σ errors. The subsequent ADF(O^{2+})'s were also in very good agreement within 1-σ errors between the simulated and actual long-slit data. In consequence, the comparison of VIRUS-P spectra with high spectral-resolution data from a long-slit in Liu et al. (1995) has provided a direct test of the validity of our analysis scheme and thus provides confidence in our abundance determinations from VIRUS-P spectra.

4.3 Maps of ORL Abundances in NGC 7009

In this section we present 2-D VIRUS-P maps of ionic abundances derived from the optical recombination line diagnostics in NGC 7009. We also detail the frequency distribution of abundance values and the radial profiles of O^{2+}/H^{+} and C^{2+}/H^{+}. The maps presented in Fig. 4.2 sample the largest spatial area of NGC 7009 to date, covering the entire bright optical core with an integral field unit (IFU) spectrograph for the first time. The spatially-resolved data here provide ORL chemical abundances over $\sim$541-arcsec^2 (corresponding to 41 VIRUS-P fiber positions). This area is $\sim$6.5 times larger than the region previously studied with another IFU, VLT FLAMES (Tsamis et al. 2008), enabling us to examine the "global" distribution of ORL abundances across the nebula, while the $\sim$50 times finer angular resolution of VLT FLAMES delivers complementary information on smaller-scale variations.

The VIRUS-P map of the O^{2+}/H^{+} ORL abundances is presented in Fig. 4.2 (b). These values are the mean of the five O II ORLs described in Section 4.1 and listed in Table 4.1. O^{2+}/H^{+} values for the individual positions are listed in Table 4.3. The most highly enhanced O^{2+}/H^{+} ORL abundances were found at positions 3, 34, and 41. Among these, position 41 is the most distant from the central star, $\sim$19$''$ along the major axis, near a region of very low surface brightness located about half way between the bright shell and the eastern ansae, also found by Liu (2003) and Liu et al. (2004). We investigate the radial variations of O^{2+}/H^{+} ORL abundances in Fig. 4.3 (a). We find an apparent gradient, with value peaking near the center, then

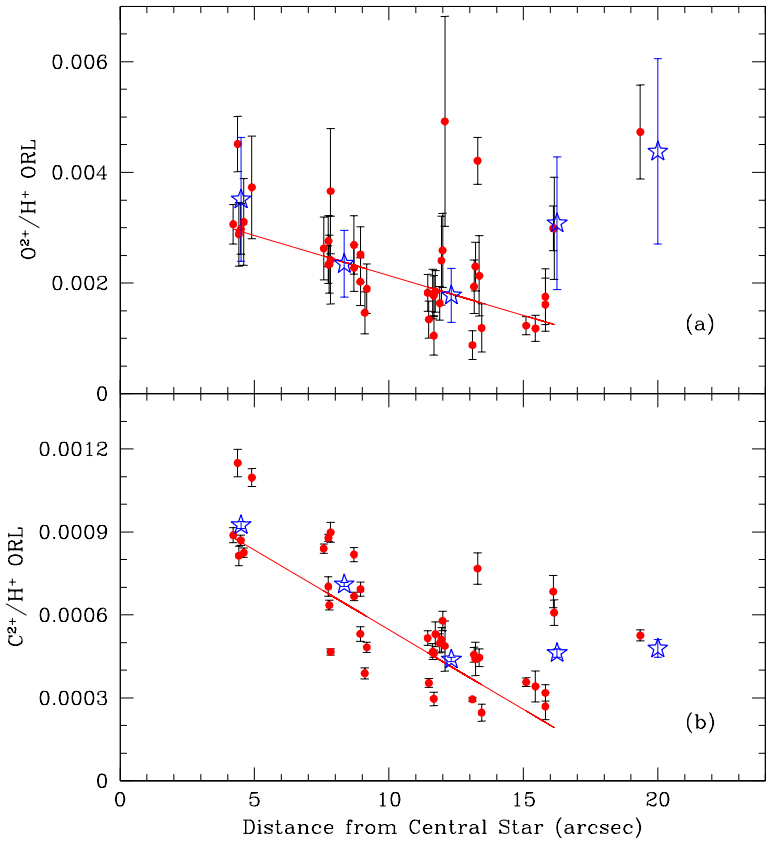

Figure 4.3 Radial profile of O^{2+}/H^{+} and C^{2+}/H^{+} ORL abundances, in (a) and (b) respectively. Each point (in red) corresponds to one of the 41 VIRUS-P positions. The error-weighted least-squares regression obtained for 40 VIRUS-P positions is indicated by the red line (see the Section 4.3 for details), and the fitting parameters are listed in Table 4.5. The radial binning has been carried out for concentric contours (blue unfilled stars; refer to Table 4.4.). Note that the small error bars for binning data are hardly seen in the bottom panel.

declining out to a distance of ∼15 arcsec from the central star. In order to increase the signal-to-noise for the weak ORLs, we carried out radial binning, by adding up VIRUS-P fibers along concentric contours from the central star. The binned data, indicated by the blue unfilled stars in Fig. 4.3 (a), shows this radial trend more clearly, at least for the central 15″. Between 16 and 20 arcsec from the central star, O^{2+}/H^{+} shows a significant upturn (these correspond to groups 4 and 5 in Table 4.4). These outer two bins have O^{2+}/H^{+} values approximately 30%, 85% higher than the mean value for all detected positions. However, the error bars for these outer, fainter positions are larger, so this upturn should be confirmed by additional observations. The larger errors associated with the outer bins may be caused by additional noise from the fibers without O II ORL detections. For 40 positions (excluding position 41 due to its singularity in chemical enrichment and distant radius), we found an error-weighted regression with a slope of -1.44×10^{-4} and an intercept of 3.582×10^{-3} (Fig. 4.3 (a) and Table 4.5). The frequency distribution of the ORL abundances shows a peak at O^{2+}/H^{+}≈2.5×10^{-3} with a wide dispersion of ∼1.0×10^{-3} (Fig. 4.4 (a)).

ORL-based abundance maps of C^{2+}/H^{+}, He^{+}/H^{+}, He^{2+}/H^{+} are presented in Fig. 4.2 (c), (d), and (e), respectively. C^{2+}/H^{+}, He^{+}/H^{+}, He^{2+}/H^{+} abundances were derived from C II λ4267, He I λ4471, He II λ4686, respectively, and the individual values listed in Table 4.3. The map of He^{+}/H^{+} in Fig. 4.2 (d) shows a rather flat spatial distribution with a mean value of (1.04±0.06)×10^{-1} (Fig. 4.4 (c)). In contrast, the spatial distribution of

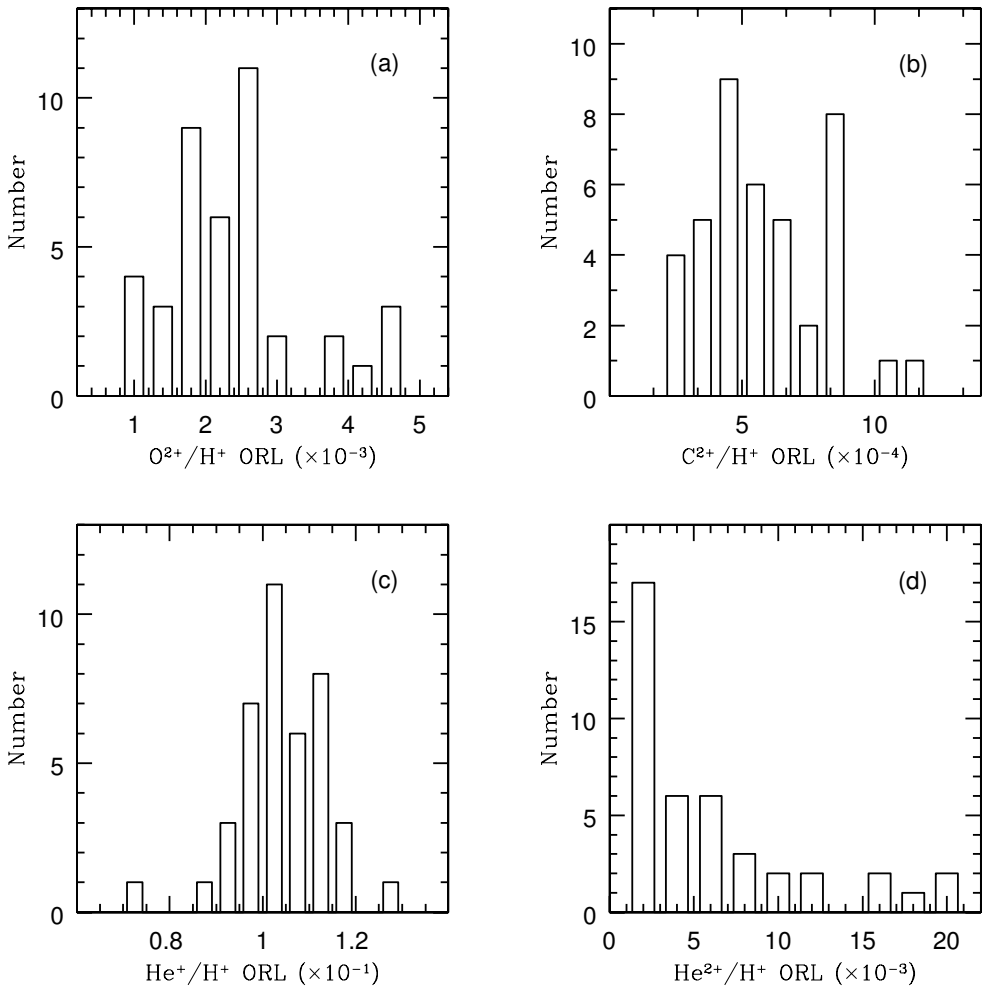

Figure 4.4 Distributions of the ORL abundances in NGC 7009, based on 41 VIRUS-P sampling positions; (a) O^{2+}/H^+ ionic abundance with a bin size $\triangle(O^{2+}/H^+)$ of 4×10^{-4}, (b) C^{2+}/H^+ abundance with $\triangle(C^{2+}/H^+)$ of 1×10^{-4}, (c) He^+/H^+ abundance with $\triangle(He^+/H^+)$ of 5×10^{-3}, and (d) He^{2+}/H^+ abundance with $\triangle(He^{2+}/H^+)$ of 2×10^{-3}.

He^{2+}/H^+ in Fig. 4.2 (e) indicates that high He^{2+}/H^+ ionic abundances are concentrated toward the nebular center, tracing the high ionization region around the central star, with a mean value of $(6.05\pm0.30)\times10^{-3}$ (Fig. 4.4 (d)). The VIRUS-P map of C^{2+}/H^+ shows high enrichment around the nebular center, with local maxima at positions 3 and 6 (Fig. 4.2 (c) and Fig. 4.4 (b)). The radial profile for the concentric contour bins discussed above for O^{2+}/H^+ is investigated in Fig. 4.3 (b). A radial C^{2+}/H^+ gradient similar to the gradient seen in O^{2+}/H^+ is established, out to a distance of 15 arcsec from the central star; i.e. larger C^{2+}/H^+ ORL abundances close to center. The error-weighted regression (red line) has a slope of -5.77×10^{-5} and an intercept of 1.123×10^{-3} (Table 4.5), fits the three central bins (innermost blue unfilled stars) well. Like the O^{2+}/H^+ radial profile, the C^{2+}/H^+ ORL abundances turn up at the outer regions between 16 and 20 arcsec, but to a more moderate extent and with smaller errors when compared to O^{2+}/H^+. This suggests that the outward upturn might be real and common to ORL lines of heavy elements in general.

4.4 Correlations

In this section we examine the correlations between various quantities based on our measurements of NGC 7009. The spatially-resolved VIRUS-P spectra offer a novel opportunity to further investigate correlations previously noted in long-slit surveys, by providing a large number of data points within a nebula. Moreover, the wide field of VIRUS-P allowed us to investigate

Y	X	Slope	Intercept	Data Points	Reference
O^{2+}/H^+ ORL	Distance (arcsec)	-1.446(-4)	3.582(-3)	40	Fig. 4.3 (a)
C^{2+}/H^+ ORL	Distance (arcsec)	-5.765(-5)	1.123(-3)	40	Fig. 4.3 (b)
C^{2+}/H^+ ORL	O^{2+}/H^+ ORL	2.173(-1)	9.327(-5)	41	Fig. 4.5 (a)
He^+/H^+ ORL	O^{2+}/H^+ ORL	1.573	1.008(-1)	41	Fig. 4.5 (b)
O^{2+}/H^+ ORL	He^{2+}/He	1.394(-2)	1.400(-3)	41	Fig. 4.5 (c)
C^{2+}/H^+ ORL	He^{2+}/He	5.012(-3)	3.435(-4)	41	Fig. 4.5 (d)
O^{2+}/H^+ ORL	I(Hβ)$\times 10^{11}$	1.060(-4)	1.420(-3)	41	Fig. 4.5 (e)
C^{2+}/H^+ ORL	I(Hβ)$\times 10^{11}$	3.961(-5)	3.028(-4)	41	Fig. 4.5 (f)
O^{2+}/H^+ CEL†	Distance (arcsec)	2.688(-5)	2.232(-4)	34	Fig. 4.6 (a) red
O^{2+}/H^+ CEL‡	Distance (arcsec)	-1.124(-5)	4.900(-4)	34	Fig. 4.6 (a) blue
ADF(O^{2+})†	Distance (arcsec)	-6.778(-1)	1.180(1)	34	Fig. 4.6 (b) red
ADF(O^{2+})‡	Distance (arcsec)	-2.942(-1)	8.959	34	Fig. 4.6 (b) blue
I(C II λ4267)/I(Hβ)	Mass Fraction (%)	1.315	1.518	41	Fig. 5.3

Table 4.5 Parameters of error-weighted regression fits. The values in parentheses correspond to the powers of 10-based exponents.
†: based on gradient T_e
‡: based on a single T_e

global trends between ORL diagnostics, by fully sampling the entire region of strong O II ORL emission in NGC 7009, which complements the higher angular resolution study of a smaller region by Tsamis et al. (2008).

A positive correlation between the ORL-based O^{2+}/H^+ and C^{2+}/H^+ abundances was established in Fig. 4.5 (a), and the error-weighted least-squares fit to the 41 VIRUS-P positions was listed in Table 4.5. The C^{2+}/H^+ ORL abundances follow the O^{2+}/H^+ ORL abundances, paralleling the positively correlated intensities between C II and O II ORLs; i.e. C II ORLs are strong where O II ORLs are strong. For a single-abundance model, this correlation could be interpreted as a consequence of temperature variations within the nebula; i.e. both C II and O II ORL intensities are enhanced where T_e is

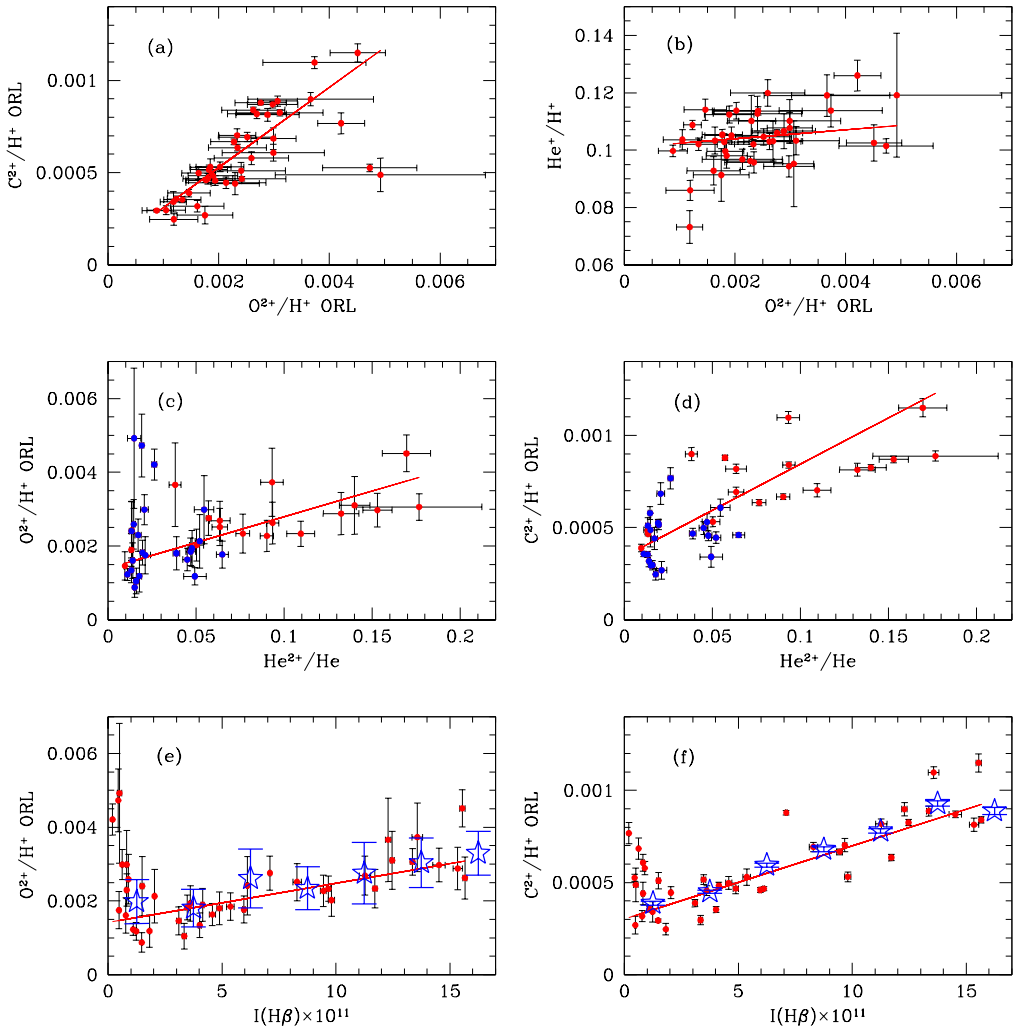

Figure 4.5 Correlations between ORL diagnostics in NGC 7009. Each data point (in red) represents one of the 41 individual VIRUS-P positions. The red solid lines are the weighted least-squares fit to these points (the fitting parameters were is listed in Table 4.5.). In (c) and (d), the red points correspond to the inner VIRUS-P positions (r<10 arcsec), while the blue points represent the outer positions (11<r<19 arcsec). The blue open stars in (e) and (f) correspond to O^{2+}/H^+, C^{2+}/H^+ ORL abundances respectively, from binned VIRUS-P spectra with a bin size $\triangle$ I(Hβ) of 2.5×10^{-11} $erg\ sec^{-1}\ cm^{-2}$ $\AA^{-1}$ (Table 4.4).

lower, due to the inversely proportional power-law dependence of ORL emissivities on temperature. However, the radial profile of ORL-based O^{2+}/H^{+}, C^{2+}/H^{+} abundances in Fig. 4.3 showed that both O II and C II ORLs become *stronger* toward the center of NGC 7009 *where* T_e *is in fact higher* (Rubin et al. 2002; the CEL T_e gradient will be discussed in the next Section 4.5). In the dual-abundance scenario, *however*, the positive correlation between C II and O II ORLs can be explained by a spatial mass fraction variation of the postulated cold, hydrogen-deficient inclusions; i.e. both C II and O II ORLs increase in strength where more of the cold material (higher mass fraction for a given angular resolution element) is concentrated.

A moderate correlation was found between He^{+}/H^{+} and O^{2+}/H^{+} in Fig. 4.5 (b); the error-weighted regression is listed in Table 4.5. A similarly weak positive trend was also found for the smaller sampling area observed with VLT FLAMES (Tsamis et al. 2008). Within the dual abundance model, the positive correlation between O^{2+}/H^{+} from the ORLs and He^{+}/H^{+} would imply that helium is also enhanced in the conjectured cold inclusions, although the He/H ratio is not very strongly constrained (Liu 2003).

In Fig. 4.5 (c) and (d), the ORL-based O^{2+}/H^{+} and C^{2+}/H^{+} ratios are compared to He^{2+}/He, and both show positive correlations (see Table 4.5). Different colors are used to distinguish the inner (r $<$ 10 arcsec; red) and outer (10 $<$ r $<$ 19 arcsec; blue) radial zones. The spatially-stratified degrees of ionization were gauged from He^{2+}/He, which traces the high ionization gas: higher He^{2+}/He values near the center (red points), and lower He^{2+}/He on

the outskirts (blue points). This trend is also seen in Fig. 4.2 (e). Overall, higher C^{2+}/H^{+} and O^{2+}/H^{+} ORL abundances are found in the higher ionization regions, suggesting that the cold, hydrogen-deficient inclusions postulated in dual-abundance model might possibly be associated with higher ionization regions in the nebula.

We plot the O^{2+}/H^{+} and C^{2+}/H^{+} ORL abundances versus the local dereddened Hβ intensity in Fig. 4.5 (e) and (f), respectively. Positive correlations are seen for both cases and the weighted regressions for 41 positions are plotted (Table 4.5). We also include the results for the binned VIRUS-P spectra with a bin size of $\triangle$I(Hβ)= $2.5{\times}10^{-11}$ $erg\ sec^{-1}\ cm^{-2}\ \mathring{A}^{-1}$ (Table 4.4), and find that they are consistent with these correlations.

We also examined the correlation between the abundance discrepancy factor (ADF) and the Hβ intensity. The ADFs, defined as ratios of the ORL-based to the CEL-based abundances, were obtained from the O^{2+}/H^{+} ORL abundances (Fig. 4.5 (e)) with the O^{2+}/H^{+} CEL abundances determined from [O III] λ4363 forbidden line in VIRUS-P spectra (details in the following Section 4.5). A similar, positive correlation as Fig. 4.5 (e) is seen between ADF(O^{2+}) and Hβ intensities. In contrast, Tsamis et al. (2008) found no clear trend between ADF(O^{2+}) and Hβ intensities for NGC 7009. One possibility is that the smaller field of VLT FLAMES, with a narrower range in Hβ intensities, obscures the trends that can be seen more clearly in a full sampling of the target with VIRUS-P. Both the presence of a positive correlation as found in our study, or the lack of a trend as found by Tsamis et al. (2008;

for both PNe NGC 7009 and NGC 5882), contradict the previous claims of an inverse correlation between ADF(O^{2+}) and Hβ intensities established for NGC 6153 (Tsamis et al. 2008). In the dual-abundance scenario, the regions emitting most of the H I ORLs (i.e. ambient hot gas) and those radiating most of the heavy element ORLs (i.e. cold, H-poor clump) do not necessarily have the same spatial distributions, and therefore there need not be a correlation between the ADFs and Hβ intensities within a nebula. The Ring Nebula, for which the O II ORLs and the Hβ intensity profile were studied by Garnett and Dinerstein (2001), has a central cavity surrounded by a bright ring in Hβ. In contrast, NGC 7009 has quite a different morphology, brighter Hβ emission close to the central star (CS) (Luo and Liu 2003). However, both studies confirm the presence of a central peak in the O II ORL abundances through long-slit observations. The spatially-resolved VIRUS-P spectra also found the similar Hβ intensity profile to Luo and Liu (2003) (i.e. centrally intensified Hβ). In the context of dual-abundance model, the correlation of ORL abundances (or ADFs) with Hβ intensity should depend on the relative spatial distributions of these two quantities within the nebula, and hence the detailed trends will differ from nebula to nebula.

4.5 CEL Abundance Determinations and ADFs

The O^+/H^+, O^{2+}/H^+ ionic abundances were derived from [O II] λ3728+3729 and the [O III] λ4363 auroral line respectively for the 41 VIRUS-P fibers. The volume emissivities of [O II] λ3728+3729, [O III] λ4363 were calculated

using a 5-level atom program (Shaw and Dufour 1994) for an electron density of n_e=4,500 cm^{-3}, a well-established average value from CEL diagnostics in earlier work on NGC 7009 (Liu et al. 1995, 2003; Hyung 1995a,b; Tsamis 2008). The adoption of a constant electron temperature, however, probably adds significant uncertainty to the CEL abundance determinations, since the CEL abundance, contrary to the ORL abundance, is very sensitive to electron temperature. Tsamis et al. (2008) found large ($\sim$1.5 times) variations in their CEL abundances even in a smaller region in the nebula, for temperature variation of $\triangle T_e$=1,100K in NGC 7009.

Although spatially-resolved T_e's are required for accurate CEL abundance determinations in the individual VIRUS-P fibers, the [O III] $\lambda\lambda$5007, 4959 nebular lines were saturated at all 41 positions (even in the short exposures) where the O II lines were detected in our data. This prevents direct determinations of [O III] nebular/auroral CEL ratios, the only T_e diagnostic available in the VIRUS-P wavelength regime. Consequently, we were unable to calculate T_e values for each fiber from our own data. However, NGC 7009 has been extensively studied for T_e variations. For example, Rubin et al. (2002) investigated the detailed temperature variations across a large area of NGC 7009, using the Hubble Space Telescope (HST)/WFPC2 narrow band images and the STIS long-slit spectroscopy, and obtained a radial profile of T_e from the forbidden line ratio [O III] λ4363/λ5007. They found gradually decreasing temperatures with increasing radius, with a change in T_e of about 1500K, from the central star to a radius of 13 arcsec, comparable to

the spatial coverage of the VIRUS-P fibers of interest. For the purpose of CEL abundance determinations, we adopted these radially-varying T_e values. Specifically, we assumed T_e=10,400K, 9,800K, 9,600K, 9,400K for the VIRUS-P positions in group 1 ($4'' <$r$<5''$), group 2 ($7'' <$r$<8''$), group 3 ($8.5'' <$r$<10''$), and group 4 ($11'' <$r$<14''$) respectively (refer to the radially-binned groups in Table 4.4). We obtained mean values of the CEL-based abundances of O^+/H^+=(1.16±0.05)×10^{-5} and O^{2+}/H^+= (4.79±0.20)×10^{-4} for all 41 fibers. Fig. 4.6 (top panel) shows the radial profile of the O^{2+}/H^+ CEL abundances for the adopted T_e's (red unfilled triangles). A positive correlation is seen between the CEL-based O^{2+}/H^+ abundance and the distance from the central star; the error-weighted regression was listed in Table 4.5. The gradient in O^{2+}/H^+ CEL abundances may reflect a real variation in O/H abundance, and/or may be caused by ionization effects. The gradient in electron temperature (Rubin et al. 2002) might be a consequence of the different concentration of O in O^{2+}, which is a more effective coolant than O^+. In other words, the lower T_e([O III]) at larger radii could result from the enhanced cooling rate produced by ionization structure. Indeed the distribution of He^{2+} which co-resides with O^{3+}, suggests that ionization effects are present. The higher ionization close to the center would convert O^{2+} into O^{3+} ions. This effect may be large enough to reduce the O^{2+}/H^+ ionic abundances as observed, in which case the higher T_e([O III]) toward the NGC 7009 nucleus can be interpreted as a consequence of the ionization effect on O^{2+} ions.

In Fig. 4.6 (a), we compare the CEL abundances derived for constant

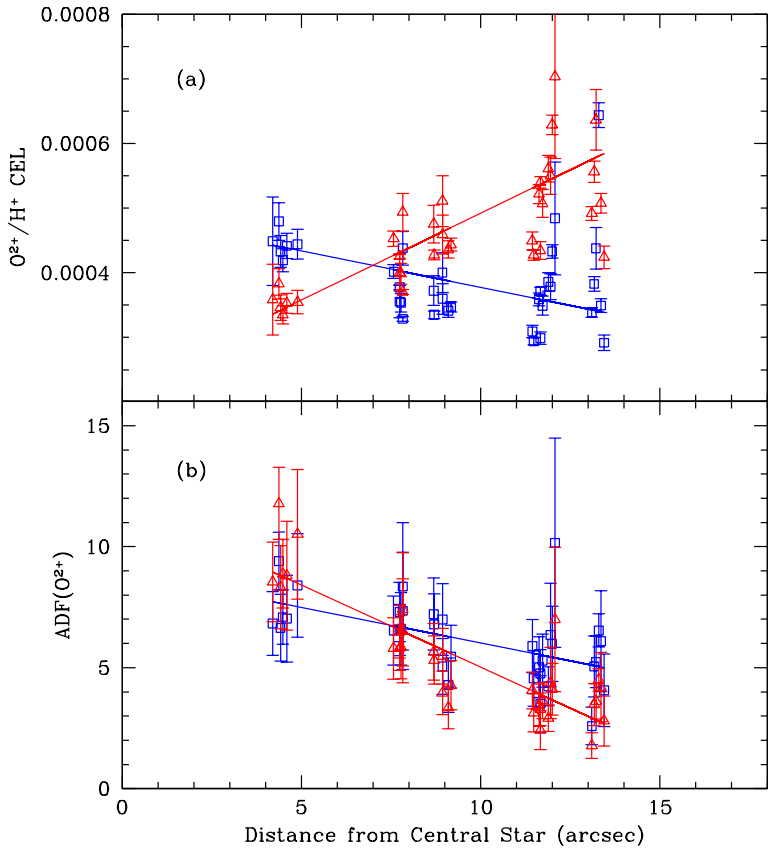

Figure 4.6 Radial profiles of the O^{2+}/H^{+} CEL abundance in (a) and ADF(O^{2+}) in (b). The red triangles correspond to the CEL-based abundances and the resulting ADFs determined with radially-varying T_e, while the blue squares correspond to the same quantities derived assuming constant T_e with radius. The red and blue solid lines comprise the error-weighted regression fits to the red triangles and blue squares respectively, and the fitting parameters were listed in Table 4.5. The radial profiles in (a) and (b) were analyzed for 34 VIRUS-P positions within r<14″, where the gradient T_e's were adopted from Rubin et al. (2002).

T_e=10^4K (blue unfilled squares) with those that take into account the radial T_e gradient of Rubin et al. (2002). The assumption of a uniform temperature causes overestimation of the CEL-based O^{2+}/H^+ abundances in the regions where the *true* T_e([O III]) is *higher* than the assumed constant T_e, and vice versa in *colder* regions. The apparent trend of an inversely varying CEL O^{2+}/H^+ with radius in Fig. 4.6 (the blue solid line in a top panel) is an artifact of this effect due to the overestimation/underestimation of the CEL abundances for "hotter" and "colder" regions respectively, and demonstrates how sensitively the CEL-derived abundances, unlike the ORL-derived abundances, depend on the electron temperature.

We obtained a mean ADF(O^{2+})=5.34±0.41 for 34 VIRUS-P positions where the CEL abundances were derived with a radially varying T_e. Fig. 4.7 shows the frequency distribution of these ADF(O^{2+}) values, in the red histogram, for a bin size of $\triangle$ADF(O^{2+})=1.00. This distribution has a peak at ∼3-6 with a maximum value of 11.8 in the central position 3 and a minimum value of 1.78 at position 28 (Fig. 4.2 (f)). The fact that the minimum ADF(O^{2+}) value is larger than unity indicates that the discrepancies between ORL and CEL abundances are ubiquitous over the entire nebula. The range of values is broad, with a dispersion of about 2.4. Large spreads in ADF(O^{2+}) within a given nebula have been noted previously (e.g. ∼5 for NGC 6720 by Garnett and Dinerstein 2001, ∼40 for NGC 6153 by Tsamis et al. 2008). Tsamis et al. found that the ADF(O^{2+}) varies with a large factor of ∼30 within the 11.5×7.2-arcsec^2 central region of NGC 7009. We found a some-

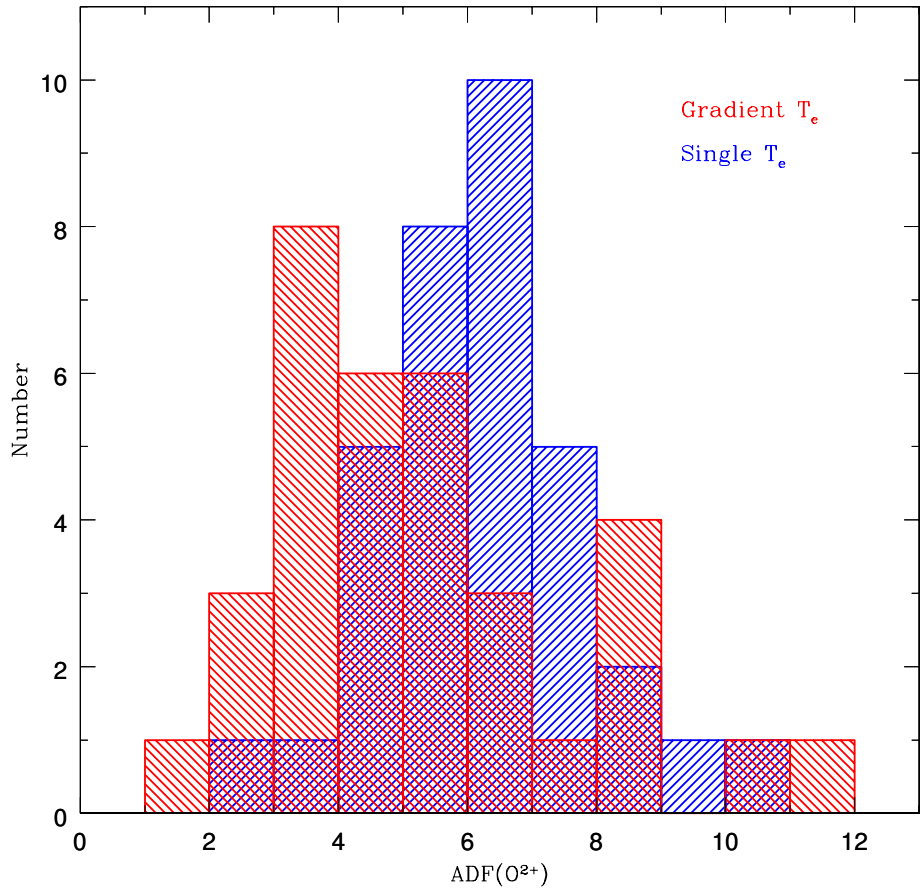

Figure 4.7 Distribution of abundance discrepancy factor (ADF) in NGC 7009, measured with VIRUS-P. The ADF(O^{2+}) with gradient T_e's (in red shaded histogram) was compared to that with a single T_e (in blue shaded histogram).

what narrower ADF(O^{2+}) variation of $\sim$7 across the 34 VIRUS-P positions representing about 5.4 times larger fields than VLT FLAMES. This may be caused by the larger angular size of each VIRUS-P fiber than that of FLAMES, which would tend to wash out small-scaled angular variations.

The radial distribution of ADF(O^{2+}) was also examined over 34 VIRUS-P positions for both cases of the CEL abundances derived with radially-varying T_e (red unfilled triangles) and with a constant temperature (blue unfilled squares), in Fig. 4.6 (b). The constant temperature case yields a shallower slope in ADF(O^{2+}) (blue solid line in Fig. 4.6 (b)) and a consequently narrower distribution in the ADF(O^{2+}) (blue histogram in Fig. 4.7). For both cases, we see an inverse correlation between ADF(O^{2+}) and the distance from the central star, despite the opposite radial dependence of the CEL O^{2+}/H^+ abundances found in Fig. 4.6 (a). It implies that the gradient in ADF(O^{2+}) primarily traces the spatially varying O^{2+}/H^+ ORL abundances, reflecting the central concentration of O^{2+} ORLs in NGC 7009. In the context of the dual-abundance model whereby the most ORLs rise from the posited component, it would require that the cold, hydrogen-deficient inclusions are more strongly concentrated in the central regions, if physical conditions (i.e. T_e, n_e, and element abundance) remain similar from clump to clump.

Chapter 5

Discussion

5.1 Overview of the Dual Abundance Model

In this section, we consider the possible physical parameters (i.e. T_e, n_e, element abundances, mass fraction) for the cold, hydrogen-deficient inclusions postulated in the dual-abundance model. The dual-abundance model proposes that these cold, metal-rich inclusions are embedded in ambient, hot ($T_e \sim 10^4$K) gas with "normal" abundances (∼solar). In this picture, most of the ORL emission arises from the cold, metal-rich clumps (due to the enriched heavy element abundances and consequent enhanced ORL emissivities at low T_e, caused by efficient cooling at high metallicity), while essentially all of the CELs originate from the hot, normal composition gas. In this chemically inhomogeneous scenario, the ORLs and the CELs yield different abundances because ORLs trace a new, highly enriched component, hidden within the predominant hot, normal gas traced by the bright CELs. In other words, the ORL/CEL discrepancy is deceptive, because the two sets of lines actually arise from material with different compositions. Viewed this way, the investigation of weak ORLs is of paramount importance because it can help reveal the physical properties of the conjectured hidden component. In the following we constrain the physical parameters (i.e. electron temperature, electron density,

element abundance, mass fraction) of the cold, hydrogen-deficient inclusions in NGC 7009, that would be consistent with our VIRUS-P spectra.

5.2 Measurements of T_e(O II ORL)

Extremely low T_e ($\lesssim 10^3$K) values have been suggested for the hydrogen-deficient inclusions in the dual-abundance model (Liu et al. 2000, Liu 2003). A radically low T_e, 10 times lower than in the ambient hot surroundings, might exist because of intense cooling of high metallicity gas in the infrared fine-structure transitions. Such a low T_e is necessary to enhance the ORL emissivities of the heavy elements, through their inversely proportional power-law dependence on T_e. Liu et al. (2000) proposed a value $T_e \sim$500K for the hydrogen-poor material in NGC 6153. Subsequently, several photoionization models have been constructed assuming two components of different abundance (Péquignot et al. 2002, 2003; Tylenda 2003).

A more recent development is that several direct measurements of the T_e in the cold inclusions have been carried out with deep long-slit spectroscopy in recent years (Liu et al. 2004, Tsamis et al. 2004, Wesson et al. 2005). These utilize as temperature diagnostics, certain weakly temperature-dependent O II line ratios, although such measurements are difficult due to the faintness of the O II ORLs. Very accurate line measurements of faint ORLs are required to derive T_e(O II ORL). For a number of surveyed PNe, T_e(O II ORL) values as low as $\lesssim$1,000K have been derived. In particular Liu et al. (2004) found T_e(O II ORL) of 1,600K for NGC 7009, when measured from the intensity

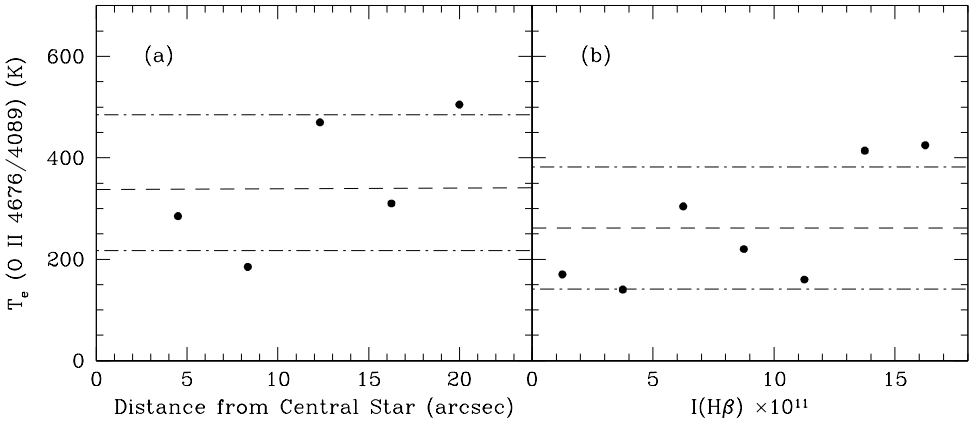

Figure 5.1 Distribution of T_e(O II ORL) in NGC 7009. The intensity ratio of O II λ4676/λ4089 was used to derive T_e(O II ORL) from the binned VIRUS-P spectra based on radial concentric contours, in (a), and Hβ intensities, in (b) (refer to Table 4.4 for detailed binning patterns). For both cases, the mean T_e(O II ORL)'s have been obtained (in dashed line) with 1-σ standard deviation (in dot-dashed line).

ratio of the O II V 1 multiplet to the 4f-3d transition λ4089 obtained from optical long-slit spectra. For the same PN, a lower T_e(O II ORL) of $\sim$500K is found from the ratio I(λ4661)/I(λ4089) reported by Bastin and Storey (2006) and the currently available O II ORL intensities published by Liu et al. (1995) and Hyung and Aller (1995a,b).

From the O II ORLs in the VIRUS-P spectra of NGC 7009, we derived T_e(O II ORL) using the intensity ratio of a 3p-3s transition, O II λ4676, to a 4f-3d transition, O II λ4089. Fig. 5.1 shows the distribution of resultant T_e(O II ORL) values derived from this ratio for the binned VIRUS-P spectra, because of their higher signal-to-noise compared to the data for individual fiber positions. We used two different binning schemes, radial contours and the Hβ intensities (Table 4.4), as shown in Fig. 5.1 (a) and (b). Both cases result in very low mean values in T_e(O II ORL) of 351K, 262K with 1-σ rms errors of 134K and 120K respectively. The radial profile of T_e(O II ORL) was examined *for the first time* for NGC 7009; no significant radial gradient in T_e(O II ORL) was found (Fig. 5.1 (a)). This implies that the postulated hydrogen-deplete inclusions have, on average, rather constant electron temperatures across the nebula. Based on our T_e(O II ORL) determinations and the previous studies using long-slit spectroscopy, we accept T_e(O II ORL)'s in a range between 300K and 1,600K as plausible electron temperatures of the posited inclusions in NGC 7009.

5.3 Constraints on n_e and Abundances

We can set a lower limit on n_e in the cold, metal-rich component from the condition that at least 0.1 per cent of total Hβ intensity originates from the hypothesized hydrogen-deficient inclusions. In a detailed photoionization model of NGC 6153 (Péquignot et al. 2002) only a few % of the H I flux originates from the cold, hydrogen-deficient inclusions, while the rest of the H I emission rise from the hot plasma occupying most of the volume. For a given value of T_e(cold gas) and measured Hβ flux, there is a relationship between the volume filling factor and n_e, that allows us to identify physically unrealistic combinations of parameters. For example, n_e as low as 100 cm^{-3} can be excluded because it results in 26%, 77% of the volume being occupied by cold material in NGC 7009, for the conditions of 0.1% and 1% Hβ intensities from such materials respectively. If we assume that no more than 0.1% of the Hβ flux comes from the cold, hydrogen-poor inclusions, this narrows the possible values of n_e for the cold component to be $n_e \gtrsim 1{,}000 cm^{-3}$ and the lower limit was set to be $n_e \geqslant 4{,}500 cm^{-3}$ which is comparable to n_e in the hotter component. In fact this low-density regime is unlikely, if the cold gas is even approximately in pressure equilibrium. Since T_e in the cold inclusions is at least 10 times lower T_e than in their hot surroundings, the corresponding density would have to be higher than in the ambient gas. Otherwise, the inclusions would collapse by the same factor as a sound-crossing time-scale, unless contraction by pressure imbalance is prevented or delayed by internal heat sources or magnetic fields within the ionized inclusions, both which are

unlikely in this case.

ORL/CEL abundance discrepancies have been well established for several elements, in particular oxygen, carbon, nitrogen, and neon. Thus, the proponents of the dual-abundance model propose that all of these elements are highly enhanced iin the cold inclusions. Liu et al. (2000) found that the best fitting of their empirical models to the observed O II ORLs in NGC 6153 indicated about 100 times enriched oxygen abundances for the cold, hydrogen-deficient inclusions, compared to "normal" oxygen abundances determined from the CELs. For a given nebula, the relative abundance ratios such as C/O, N/O and Ne/O derived from the ORLs are similar to those from the CELs, yielding similar ADF values for those heavy elements (Liu et al. 2000, Luo et al. 2001, Liu et al. 2004). In fact, highly enriched abundances in heavy elements, such as O, C, N, Ne, are the key feature that fundamentally distinguishes the dual-abundance model from other proposed explanations of the ADF phenomenon (e.g. temperature fluctuation, density inhomogeneities). The posited enrichments in heavy elements lead naturally to low temperatures (due to enhanced cooling) and strong ORL emission, which apparently cause the ADF problem. Meanwhile, the temperature fluctuations or density inhomogeneities with homogeneous abundances hypotheses attribute the ORL/CEL discrepancy to underestimation of the CEL abundances (due to the overestimation of T_e). In the density inhomogeneties scenario (Viegas and Clegg 1994), for example, dense condensations with $n_e \gtrsim 10^6 cm^{-3}$ collisionally suppress the [O III] $\lambda\lambda$4959,5007 CELs for which n_{crit}=6.9$\times 10^5 cm^{-3}$, while the

[O III] λ4363 forbidden line for which n_{crit}=2.5$\times10^7 cm^{-3}$ is hardly affected. This differential suppression then would lead to the overestimation of T_e, when measured from the diagnostic CEL ratio [O III] $\lambda\lambda$(4959+5007)/λ4363, and therefore the underestimation of the CEL abundances, giving rise to a large ADF. Therefore, the density inhomogeneties scenario predicts a dependence of ADFs on the critical densities of the CELs. However, Liu et al. (2000), Tsamis et al. (2004) and Liu et al. (2004) do not find any such dependences among a large set of UV, optical, and IR CELs and consequently rule out the density inhomogeneities explanation. Such constraints (i.e. the dependence of ADFs on the critical density of CELs) do not apply to the dual-abundance model, since the very low T_e ($\lesssim 10^3 K$) caused by enhanced cooling of metal-rich component would significantly suppress most CELs and hence essentially no optical and UV CELs would arise from the cold, hydrogen-deficient inclusions. Thus, the lack of dependence of ADFs on n_{crit} of the various CEL diagnostics is compatible with the dual-abundance model, and at the same time does not rule out the possibility of high densities ($n_e \gtrsim 10^6 cm^{-3}$) in the cold, hydrogen-deficient inclusions. Liu et al. (2006b) measured the observed ratio of relative intensities of O II multiplet V1, which traces the *true* T_e and n_e of cold, hydrogen-deficient inclusions, for the southern planetary nebula Hf 2-2 with the highest ADF to date ($\gtrsim$70). They found an electron temperature of $\sim$630K, and electron density of $\lesssim 10^4$ cm^{-3}, and concluded that there is no observational evidence of substantial high-density condensation with $n_e \gtrsim$ 10^5-10^6 cm^{-3}.

5.4 Plausible Physical Conditions through Cloudy Modelling

In order to constrain the electron density and element abundance, we ran the photoionization model Cloudy (Ferland et al. 1998; version 07.02.01). The continuum ionizing source was set to be a blackbody with T=80,000K and L=3,136$L_{\odot}$ (Gonçalves et al. 2006). A spherical shell model was specified, with different values of electron density n_e in a grid ranging from 4,500 to $10^5 cm^{-3}$, selected to be the electron densities comparable to the ambient gas and approximately equivalent to the pressure equilibrium. The O, C, N, Ne element abundances for the cold, hydrogen-deficient component were chosen to have three different values: 10, 50, 100 times the hot gas CEL abundances in NGC 7009 (C, N, O CEL abundances from Liu et al. 1995; Ne CEL abundance from Luo et al. 2001). We ran models for VIRUS-P fiber positions at several different radii: r = 4.5, 8.3, 12.3, 16.3 arcsec for a distance of 0.86 kpc (Fernández et al. 2004). We examined the equilibrium temperatures for each combination of n_e and element enrichments in the cold inclusions at different distances from the central ionizing source.

Fig. 5.2 shows the resultant equilibrium temperatures of the cold, hydrogen-deficient inclusions for different values of n_e and element abundances at 12.3 arcsec from the CS. The variations in T_e within such cold, hydrogen-poor components were plotted as a function of the radial depth within the inclusions, with a range from 0.1 AU (near the ionization front) to 1000 AU (the maximum physical size of the posited inclusions; Tsamis et al. 2008).

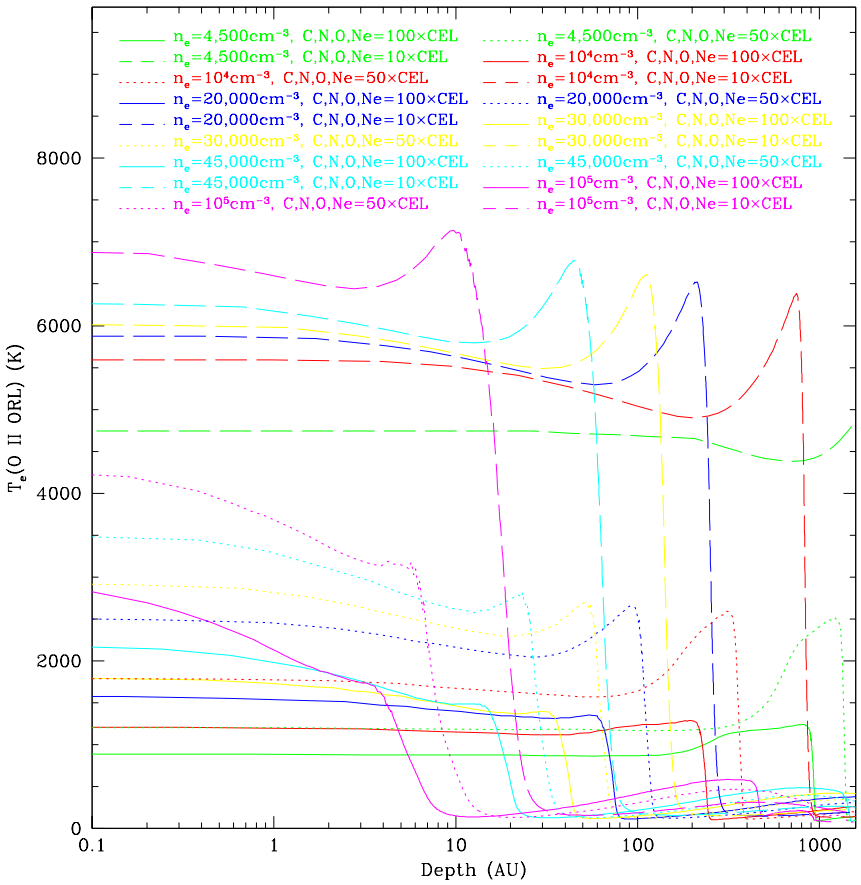

Figure 5.2 Cloudy modelling of the physical conditions in the cold, metal-rich inclusions postulated in the dual-abundance model. The variations in electron temperatures were plotted as a function of depth in the inclusions (i.e. ionization front on the left, inward distance in the clumps toward the right). Clumps at different distances from the central star (CS) of NGC 7009 have been modeled, matching the VIRUS-P fiber positions. The plot above corresponds to the clumps located at r = 12.3 arcsec from the CS. The different colors indicate the different n_e's: 4,500 cm^{-3} (green), $10^4 cm^{-3}$ (red), $2 \times 10^4 cm^{-3}$ (blue), $3 \times 10^4 cm^{-3}$ (yellow), 45,000 cm^{-3} (cyan), and $10^5 cm^{-3}$ (magenta), respectively. The different lines represent different element abundances in C, N, O, Ne; i.e. the solid lines are for 100 times enhancements of CEL abundances, the dotted lines for 50 times, and the long-dashed lines for 10 times enrichments, respectively.

First of all, in Fig. 5.2, neither 10 times nor 50 times of enhancements in C, N, O, Ne element abundances has successfully reproduced the low T_e values, $\leqslant$ 1600K over the conjectured inclusions with a maximum size of 1000 AU. On the other hand, gas with 100 times enriched heavy elements resulted in a sufficiently low T_e value for n_e=4500, 10^4, and 2×10^4 cm^{-3} (corresponding to green, red, and blue solid lines in Fig. 5.2). This indicates that extremely high enrichments (i.e. $\sim$100 times of "normal" abundances) in heavy elements (e.g. C, N, O, Ne) are essential to reach the low T_e values. Secondly, near the ionization front (corresponding to the small depth (AU) in Fig. 5.2), higher n_e clumps have higher equilibrium T_e, and vice versa (i.e. the lower n_e, the lower T_e). This correlation of T_e with n_e is caused by the dependence of the CEL cooling rate on n_e; i.e. the CEL emissivity is proportional to n_e for $n_e<n_{crit}$ but independent of n_e for $n_e>n_{crit}$, while heating due to photoionization is proportional to n_e. Meanwhile, toward the deep inside of the cold inclusions, the enhanced cooling of metal-rich component (controlled by far-IR fine structure lines) drops the equilibrium temperature efficiently. Based on T_e's ranging between 300K to 1,600K, we selected tenable electron densities and element abundances for the cold, hydrogen-deficient component in NGC 7009. It should be noted that the selected combinations of n_e and O, C, N, Ne abundances have reproduced the low temperatures of T_e ($\sim$ 300K to 1,600K) at all fiber positions over the four simulated distances from the CS.

Parameter	Model 1	Model 2	Model 3	Model 4
Component 1 (Hot and "Normal")				
n_e (cm^{-3})		4,500		
T_e (K)		10^4		
O/H		4.07×10^{-4}		
C/H		1.32×10^{-4}		
N/H		1.26×10^{-4}		
Ne/H		1.74×10^{-4}		
Volume Filling Factor (%)	99.26	99.93	99.99	99.99
Mass Fraction (%)	61.3	87.9	94.4	95.8
Component 2 (Cold and metal-rich)				
n_e (cm^{-3})	4,500	10^4	2×10^4	3×10^4
T_e (K)	1032	417	342	369
O/H		407×10^{-4}		
C/H		132×10^{-4}		
N/H		126×10^{-4}		
Ne/H		174×10^{-4}		
Volume Filling Factor (%)	7.36×10^{-1}	6.56×10^{-2}	1.38×10^{-2}	6.70×10^{-3}
Mass Fraction (%)	38.7	12.1	5.6	4.2
I(Hβ) Comp1:Comp2	22.82:1	26.86:1	28.84:1	26.22:1
I(O II λ4089) Comp1:Comp2	0.143:1	0.142:1	0.140:1	0.138:1
I([O III] λ4363) Comp1:Comp2	1.03×10^{23}:1	1.51×10^{24}:1	1.80×10^{24}:1	1.65×10^{24}:1

Table 5.1 Plausible physical conditions of cold, metal-rich inclusions in NGC 7009. The component 2 corresponds to the posited cold, metal-rich inclusions embedded in ambient, hot and "normal" gas (denoted by component 1).

5.5 Volume Filling Factor and Mass Fraction

Four sets of possible physical conditions for the cold, hydrogen-deficient and metal-rich components were found and listed in Table 5.1. They all have 100 times enriched O, C, N, Ne element abundances and very low temperatures, between 350 and 1000K over the maximum clump size of 1000 AU. The electron densities span from 4,500 cm^{-3} (model 1) to 3×10^4 cm^{-3} (model 4). For a given set of physical conditions, the volume filling factor f of the cold, hydrogen-deficient inclusions was derived for the individual VIRUS-P fiber positions,

$$\begin{aligned}\frac{I_{blend}(ORL)}{I(H\beta)} &= \frac{\lambda(H\beta)}{[\alpha_\beta(T_2,n_2)\cdot n_2^2\cdot f+\alpha_\beta(T_1,n_1)\cdot n_1^2\cdot(1-f)]}\times \\ &\sum_i[\lambda_i^{-1}\cdot[\alpha_i(T_2,n_2)\cdot(O^{2+}/H^+)_2\cdot n_2^2\cdot f \\ &+\alpha_i(T_1,n_1)\cdot(O^{2+}/H^+)_1\cdot n_1^2\cdot(1-f)]] \qquad (5.1)\end{aligned}$$

where the subscript 1 stands for the hot, "normal" component, 2 for the cold, hydrogen-deficient component, and α_β, α_i are the effective recombination coefficients of Hβ and individual O II ORLs within the blends, respectively. The quantities f and (1-f) are the volume filling factors of the cold inclusions and the hot gas in each VIRUS-P fiber along the line-of-sight, respectively. The contributions of both cold and hot components to the intensities of the O II and H I recombination lines have been taken into account. Therefore, for given values of T_e, n_e, and the element abundance, the observed intensity ratios of O II ORLs relative to Hβ depend on the reciprocal volume occupied by the cold and hot components. We found f and (1-f) from the five O II ORLs for 41 individual VIRUS-P fibers; the averaged values are listed in Table 5.1 for four

empirical models. In all cases, the averaged volume filling factors f's of cold, hydrogen-poor inclusions were much smaller than those of ambient hot component. Model 1 resulted in the minimum f of 7.36×10^{-3} (with an associated (1-f) of 99.26 % for the hot gas), and the values of f decrease for the latter models (e.g. f of 6.70×10^{-5} for model 4). These decreasing f's are caused by the increasing electron densities in the latter models; i.e. the intensities of O II ORLs are much more intensified in latter models with higher n_e (due to the dependence of ORL intensities on n^2), and consequently a smaller value of f is sufficient to fit the observed intensities of O II ORLs, given for similar T_e and heavy element abundances.

We then derived the mass fraction of oxygen, defined as the ratio of the mass of the cold, metal-rich inclusions to the total oxygen mass. Individual mass fractions for the 41 fiber positions (for model 4) and the averaged values for four different models are listed in Table 4.3 and Table 5.1, respectively. As shown in Table 5.1, the mass fractions of the cold, hydrogen-deficient inclusions decrease from model 1 to model 4 (according to their decreasing volume filling factors). Average mass fractions of 38.7 %, 12.1 % were obtained for models 1 and 2 respectively, while 5.6 %, 4.2 % of mass fractions were found for model 3 and model 4, respectively. A mass fraction as high as 38.7 per cent is hardly plausible for the cold inclusions hypothesized in the dual-abundance model. Much lower (about a few per cent) mass fractions were proposed for the postulated cold inclusions in the photoionization models of the chemically inhomogeneous PNe (Tylenda 2003). We favor models with low mass fractions,

model 3 and model 4, which have ∼5 % of the mass in the cold, hydrogen-deficient inclusions. The inclusions are also the closest to being in pressure equilibrium with the ambient surroundings, for these models.

5.6 Contributions of the Two Phases to ORLs and CELs

We further examined the intensity ratios of the hot, "normal" gas (component 1) relative to the cold, hydrogen-deficient inclusions (component 2) for Hβ, O II λ 4089 ORL, and [O III] λ4363 CEL in Table 5.1. For all of the models, the [O III] λ4363 CEL was overwhelmingly dominated by the hot, diffuse component, which has approximately 10^{23} to 10^{24} times stronger CEL emission than the cold component. The fact that essentially no CEL emission arises from the cold, metal-rich component is due to two effects; (i) CEL emission is severely suppressed at such low temperatures, and (ii) the negligible volume and mass fractions of the inclusions. We also found that the most of the Hβ flux came from the ambient, diffuse nebular gas (component 1), whilst only a few per cent of it originated from the hydrogen-deficient inclusions (component 2), for all empirical models in Table 5.1. A few per cent of Hβ flux coming from the cold, hydrogen-poor inclusions is consistent with the photoionization model incorporating the metal-rich component conjectured in dual-abundance model (Péquignot et al. 2002). They are also compatible with the previously assumed condition on the Hβ intensity, to constrain the lower limit on n_e (i.e. at least 0.1 per cent of total Hβ intensity comes from the hypothesized hydrogen-deficient inclusions.). As for the O II ORLs, we

investigated the relative intensity ratio of O II λ4089 between hot (component 1) and cold (component 2) gases. We found, for all empirical models, that a majority ($\sim$90 per cent) of O II ORL intensity originates from the cold, metal-rich inclusions while only minor portion rises from the hot, diffuse gas. It is noteworthy that having 90 per cent of ORLs come from the cold, metal-rich inclusions is "moderate", compared to the "overwhelming ($\sim$100 per cent)" emission of the CELs from hot, diffuse gas. The "moderate" dominance in the ORL flux from the cold, hydrogen-deficient inclusions mainly results from their tiny volume and mass fractions (compared to the huge fractions of the hot diffuse gas), in spite of the enhanced heavy element abundances and the highly reinforced radiative recombination coefficients per unit volume at such a low $T_e \lesssim$ 1,000K.

5.7 C II Intensity versus Oxygen Mass Fraction

Assuming the above specified properties for the cold inclusions, we investigated the correlation between the mass fraction and the observed C II λ4267 ORL intensity. Fig. 5.3 shows that the C II λ4267 ORL intensity correlates positively with the oxygen mass fraction in the cold phase. This indicates that the C II ORL intensity is enhanced where O II lines are stronger. In the context of dual-abundance model, the heavy element ORL intensity (e.g. C II ORL) should be reinforced in the regions with higher mass fractions of cold, metal-rich materials, as long as the relative abundance ratio between heavy elements of interest (e.g. C/O, N/O, Ne/O) remains constant across

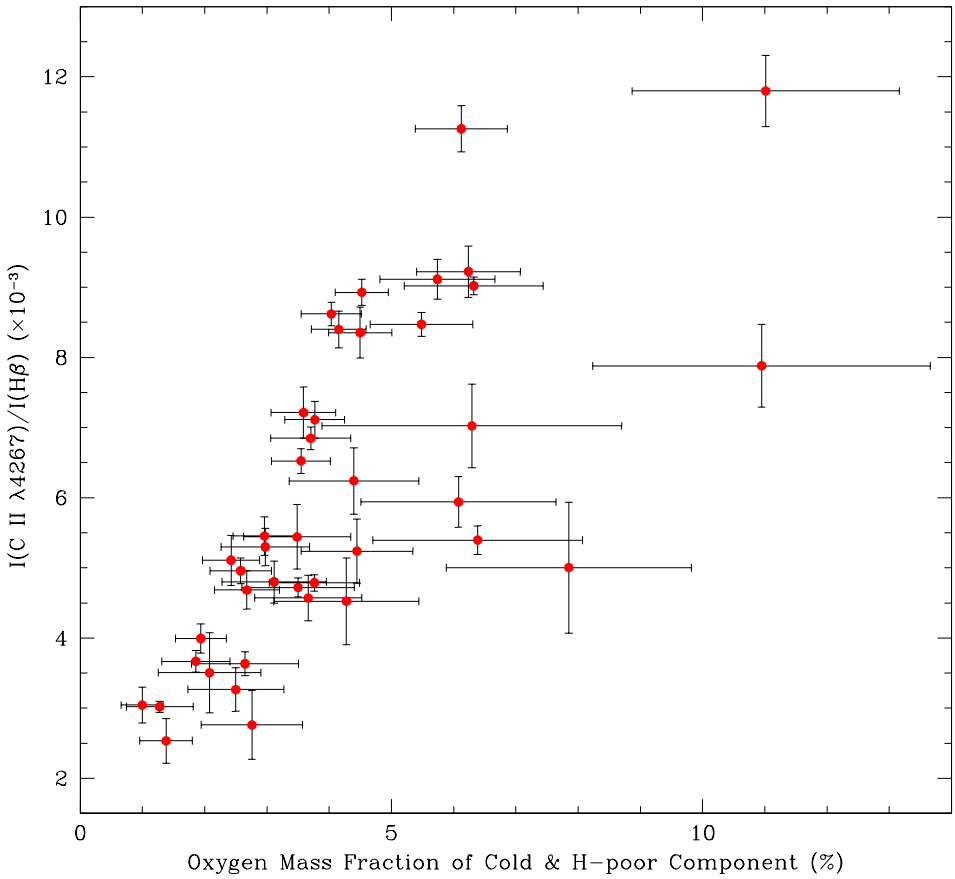

Figure 5.3 Correlation between the intensity ratio of C II λ4267 to Hβ and the mass fraction of cold, metal-rich inclusions determined from the O II ORLs in VIRUS-P spectra. The oxygen mass fraction was calculated for model 4 in Table 5.1 (refer to the Section 5 for details.). Each point (in red) corresponds to 41 individual VIRUS-P positions in NGC 7009 and the weighted least-squares regression was listed in Table 4.5.

the nebula.

5.8 The Origin of the Posited Cold, H-Poor Inclusions

The origin of the postulated cold, hydrogen-deficient inclusions is not clear at the moment. Some suggestions include (i) circumstellar material in the form of a disc-torus structure, (ii) evaporating dusty 'cometary knots', (iii) recently ejected gas from the nucleus, and (iv) evaporation of the planetary system of the progenitor star (Liu 2003; Liu et al. 2004; Tsamis et al. 2008).

Circumstellar structure, case (i), has been recently discovered very close to the star in the planetary nebula Mz 3 (Chesneau et al. 2007), with an estimated radius of < 1000 AU. Such circumstellar materials are found to contain large amounts of silicate dust and the C/O ORL abundance ratio is less than unity. The spatial distribution of O and C ORL abundances found in our study of NGC 7009 suggests that the metal-rich component is highly enhanced in the vicinity of the central star, and a small circumstellar disk or torus would have this property. In the PNe studied with spatially resolved measurement of ORLs so far, which include NGC 4361 (Liu 1998), NGC 6153 (Liu et al. 2000), NGC 6720 (Garnett and Dinerstein 2001) and NGC 7009 (Luo and Liu 2003), the ORL abundances are found to have in common large radial gradients, peaking strongly at the central star.

Cometary knots, case (ii), have long been known to exist in the Helix Nebula (O'Dell et al. 2002, 2007), and have been suggested as a source of the cold, metal-rich inclusions. However, at least in the Helix Nebula, the

cometary knots are located far from the central star, in contrary to the centrally enhanced behavior found in our study of NGC 7009. In fact they are mainly in the form of molecules, and therefore one would need a physical process that could destroy the molecular hydrogen and ionize the heavy elements so that they could produce the ORLs. Spatially-resolved observations, similar to that in this paper, should answer these question more clearly.

H-poor knots, case (iii), have been observed in Abell 30 or Abell 58 (Borkowski et al. 1993; Guerrero and Manchado 1996). They might be ejected from the central star after undergoing a late helium-flash (Iben et al. 1983). If such knots are the origin of the enhanced ORL abundances, they could reflect the evolutionary state of the PNe, because such knots would be more readily observed as the nebulae evolve (in other words, the density and the temperature contrast get more significant, compared to the ambient environments, in the more evolved PNe).

Evaporation of a planetary system (terrestrial planets, comets, asteroid, etc.), case (iv), has also been suggested as the origin of cold, metal-rich inclusions (Liu 2003). Recently many stars are found to harbor planets. Based on the (oxygen) mass fraction of a few per cent of total mass, multiple giant planets, or 'Hot Jupiters' with masses of order 10^{30} g (Marcy et al. 2005), could be a candidate for this possibility.

Chapter 6

Summary

We carried out the spatially-resolved observations of NGC 7009, utilizing the integral field spectrograph Visible Integral-field Replicable Unit Spectrograph-Prototype (VIRUS-P) on the McDonald Observatory 2.7-m telescope. Spectra were obtained over the wavelength range $\lambda\lambda$ 3550-5850 with a spectral resolution of FWHM$\sim 5\mathring{A}$, across the full VIRUS-P sampling field (112×112-$arcsec^2$) with an angular resolution of $4''.1$ per fiber. Several O II ORLs were detected in 41 VIRUS-P fiber positions, along with recombination and collisionally excited lines of other ions. We determined O^{2+}/H^+ ORL abundances from five O II ORLs: i.e. the 4f-3d transitions $\lambda\lambda$4089, 4275, 4282, 4303, and the 3p-3s transition λ4676. The C^{2+}/H^+, He^+/H^+, He^{2+}/H^+ abundances were derived from ratios among C II λ4267, He I λ4471, He II λ4686, and Hβ λ4861. The empirical radial gradients in the O^{2+}/H^+ and C^{2+}/H^+ ORL abundances were established, peaking toward the central star. A similar trend was found in ADFs: the radially increasing ADFs toward the NGC 7009 central star.

Our investigation into the ORL and CEL intensity ratios finds that the data can be explained by the dual-abundance scenario, although the cold,

metal-rich inclusions have not yet been directly observed. We compute physical conditions which would successfully reproduce our observations. Based on analysis of observed O II ORLs in our VIRUS-P spectra, we find that the cold, hydrogen-deficient and metal-rich inclusions postulated in the dual-abundance model would have to have $T_e \sim 350$K, $n_e =$ a few$\times 10^4 cm^{-3}$ with heavy element abundances of $\sim 100\times$solar, and would occupy about 10^{-4} of total volume and constitute a few per cent of the total oxygen mass in NGC 7009.

Appendix

Appendix 1

Volume Filling Factor and Mass Fraction

1.1 Volume Filling Factor (Unblended Lines)

Each of the VIRUS-P fibers can be regarded as a cylindrical column along the line of sight (Fig. 1.1), where the hot and "normal-abundance" component will be designated by subscript 1, and the cold, hydrogen-deficient component by subscript 2. Let the electron temperature, electron density, and ionic abundance of the hot component be T_1, n_1, $(O^{2+}/H^+)_1$, while those of the cold component are T_2, n_2, $(O^{2+}/H^+)_2$. Then, let the the volume filling factor of the cold component be f and the corresponding volume fraction of the hot component will be (1-f), as shown in Fig. 1.1.

Fig. 1.2 shows the schematic emission lines from the nebula. In the

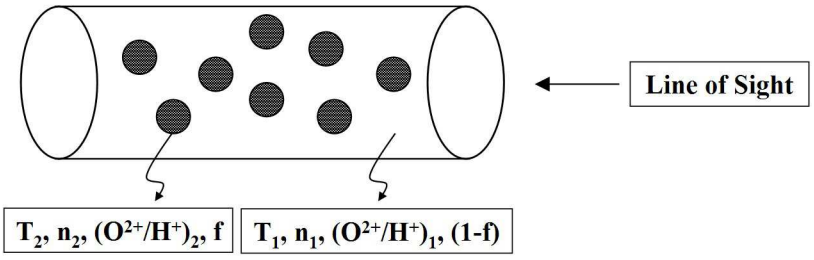

Figure 1.1 A schematic of cold, hydrogen-deficient inclusions (represented as the crosshatch) embedded in hot, "normal" gas, in the VIRUS-P fiber.

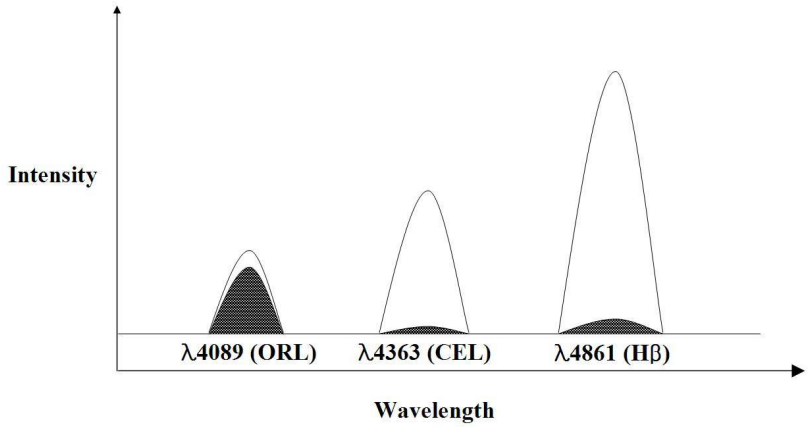

Figure 1.2 Schematic emission spectra of ORL, CEL, and Hβ. The fluxes coming from the cold, hydrogen-deficient inclusions are represented in the crosshatch.

single abundance case, all emission lines simply originate from one single component (that is, hot, "normal-abundance" component). In the dual-abundance case, however, the observed emission lines simultaneously come from both hot and cold components, both of which contribute in each cylindrical column of fiber. Since the intrinsic condition of the hypothesized secondary components in dual-abundance model is cold and metal-rich (also note that the radiative recombination coefficients get stronger in such conditions), the ORLs have a major contribution from component 2. Meanwhile, the CELs will virtually be produced only by hot and "normal" component, because the contribution of cold and metal-rich component to CELs can be ignored (or is very minor). From this point of view, therefore, the ORLs are critical for diagnosing conditions in the posited cold inclusions.

We can calculate the volume filling factor f of cold component (with

subscript 2) from the observed ORLs and H recombination lines (e.g. Hβ), as follows. First, the ORL flux originating from the cold component is

$$\begin{aligned} I_{(OLR,2)} &= \frac{hc}{\lambda_{(ORL)}} \cdot \alpha_{(ORL)}(T_2, n_2) \cdot n_e n_{O^{2+}} \cdot f \\ &\approx \frac{hc}{\lambda_{(ORL)}} \cdot \alpha_{(ORL)}(T_2, n_2) \cdot (\frac{O^{2+}}{H^+})_2 \cdot n_2^2 \cdot f \end{aligned} \tag{1.1}$$

In the same manner, the ORL flux from the hot component is

$$I_{(OLR,1)} \approx \frac{hc}{\lambda_{(ORL)}} \cdot \alpha_{(ORL)}(T_1, n_1) \cdot (\frac{O^{2+}}{H^+})_1 \cdot n_1^2 \cdot (1-f) \tag{1.2}$$

Then the observed ORL flux is the combination of fluxes from the two components

$$\begin{aligned} I_{(ORL)} &= I_{(ORL,1)} + I_{(ORL,2)} \\ &\approx \frac{hc}{\lambda_{(ORL)}} \cdot [\alpha_{(ORL)}(T_2, n_2) \cdot (\frac{O^{2+}}{H^+})_2 \cdot n_2^2 \cdot f \\ &\quad + \alpha_{(ORL)}(T_1, n_1) \cdot (\frac{O^{2+}}{H^+})_1 \cdot n_1^2 \cdot (1-f)] \end{aligned} \tag{1.3}$$

The same formula applies for Hβ

$$\begin{aligned} I_\beta &= I_{(\beta,1)} + I_{(\beta,2)} \\ &\approx \frac{hc}{4861} \cdot [\alpha_\beta(T_2, n_2) \cdot n_2^2 \cdot f \\ &\quad + \alpha_\beta(T_1, n_1) \cdot n_1^2 \cdot (1-f)] \end{aligned} \tag{1.4}$$

Therefore, the observed flux ratio would be

$$\begin{aligned} \frac{I_{(ORL)}}{I_\beta} = \frac{4861}{\lambda_{(ORL)}} &\cdot [\alpha_\beta(T_2, n_2) \cdot n_2^2 \cdot f + \alpha_\beta(T_1, n_1) \cdot n_1^2 \cdot (1-f)]^{-1} \\ &\cdot [\alpha_{(ORL)}(T_2, n_2) \cdot (O^{2+}/H^+)_2 \cdot n_2^2 \cdot f \\ &\quad + \alpha_{(ORL)}(T_1, n_1) \cdot (O^{2+}/H^+)_1 \cdot n_1^2 \cdot (1-f)] \end{aligned} \tag{1.5}$$

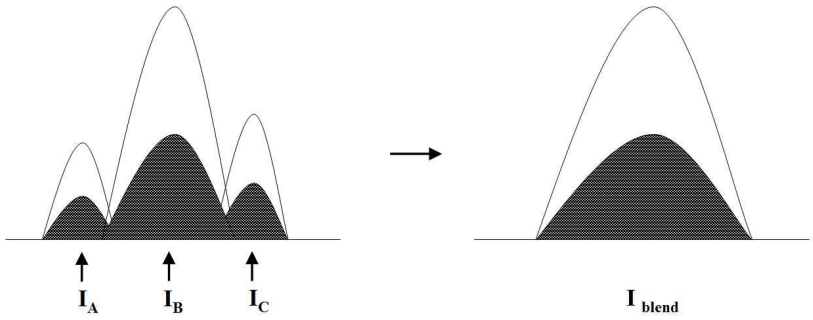

Figure 1.3 The schematic of the adjacent, individual lines (left), and their blends (right).

1.2 Volume Filling Factor (Blended Lines)

The actual situation in the VIRUS-P spectra is a bit more complicated due to its low-spectral resolution ($\lambda/\triangle\lambda \sim$1000 at 5000$\mathring{A}$). In fact, the ORLs of our interest are all blended to some extent, and we need to develop the discussion in the previous section to apply to the blended ORLs.

Fig. 1.3 shows the schematic blended ORLs in VIRUS-P spectra. Lets consider a simple case of 3-blended lines (so that we can easily extend it to n-blended lines later), and lets call them with subscripts A, B, and C. Then the flux from each individual ORL will be

$$\begin{aligned}\frac{I_A}{I_\beta} = \frac{4861}{\lambda_A} \quad &\cdot \quad [\alpha_\beta(T_2, n_2) \cdot n_2^2 \cdot f + \alpha_\beta(T_1, n_1) \cdot n_1^2 \cdot (1-f)]^{-1} \\ &\cdot \quad [\alpha_A(T_2, n_2) \cdot (O^{2+}/H^+)_2 \cdot n_2^2 \cdot f \\ &\qquad +\alpha_A(T_1, n_1) \cdot (O^{2+}/H^+)_1 \cdot n_1^2 \cdot (1-f)]\end{aligned}$$

$$\frac{I_B}{I_\beta} = \frac{4861}{\lambda_B} \cdot [\alpha_\beta(T_2, n_2) \cdot n_2^2 \cdot f + \alpha_\beta(T_1, n_1) \cdot n_1^2 \cdot (1-f)]^{-1} \cdot [\alpha_B(T_2, n_2) \cdot (O^{2+}/H^+)_2 \cdot n_2^2 \cdot f + \alpha_B(T_1, n_1) \cdot (O^{2+}/H^+)_1 \cdot n_1^2 \cdot (1-f)]$$

$$\frac{I_C}{I_\beta} = \frac{4861}{\lambda_C} \cdot [\alpha_\beta(T_2, n_2) \cdot n_2^2 \cdot f + \alpha_\beta(T_1, n_1) \cdot n_1^2 \cdot (1-f)]^{-1} \cdot [\alpha_C(T_2, n_2) \cdot (O^{2+}/H^+)_2 \cdot n_2^2 \cdot f + \alpha_C(T_1, n_1) \cdot (O^{2+}/H^+)_1 \cdot n_1^2 \cdot (1-f)] \quad (1.6)$$

By summing up all above, the blended flux will be

$$\begin{aligned}\frac{I_{blend}}{I_\beta} = \frac{I_A + I_B + I_C}{I_\beta} &= \frac{4861}{[\alpha_\beta(T_2, n_2) \cdot n_2^2 \cdot f + \alpha_\beta(T_1, n_1) \cdot n_1^2 \cdot (1-f)]} \times \\ &[\lambda_A^{-1} \cdot [\alpha_A(T_2, n_2) \cdot (O^{2+}/H^+)_2 \cdot n_2^2 \cdot f \\ &+\alpha_A(T_1, n_1) \cdot (O^{2+}/H^+)_1 \cdot n_1^2 \cdot (1-f)] \\ &+\lambda_B^{-1} \cdot [\alpha_B(T_2, n_2) \cdot (O^{2+}/H^+)_2 \cdot n_2^2 \cdot f \\ &+\alpha_B(T_1, n_1) \cdot (O^{2+}/H^+)_1 \cdot n_1^2 \cdot (1-f)] \\ &+\lambda_C^{-1} \cdot [\alpha_C(T_2, n_2) \cdot (O^{2+}/H^+)_2 \cdot n_2^2 \cdot f \\ &+\alpha_C(T_1, n_1) \cdot (O^{2+}/H^+)_1 \cdot n_1^2 \cdot (1-f)]] \quad (1.7)\end{aligned}$$

Ansatz, the general equation for n-blended ORLs is

$$\begin{aligned}\frac{I_{blend}}{I_\beta} = \frac{\sum I_i}{I_\beta} &= \frac{4861}{[\alpha_\beta(T_2, n_2) \cdot n_2^2 \cdot f + \alpha_\beta(T_1, n_1) \cdot n_1^2 \cdot (1-f)]} \times \\ &\sum_{i=1}^{n} [\lambda_i^{-1} \cdot [\alpha_i(T_2, n_2) \cdot (O^{2+}/H^+)_2 \cdot n_2^2 \cdot f \\ &+\alpha_i(T_1, n_1) \cdot (O^{2+}/H^+)_1 \cdot n_1^2 \cdot (1-f)]] \quad (1.8)\end{aligned}$$

Consequently, for a given pair of physical properties (T_1, n_1, $(O^{2+}/H^+)_1$) and (T_2, n_2, $(O^{2+}/H^+)_2$), the volume filling factor f of the H-poor component and (1-f) of the normal component are calculated for each ORL of interest, from Equation (1.8).

1.3 Mass Fractions

With a calculated volume fraction f, I define the mass fraction f_M (in oxygen) as a ratio of the total mass of O in cold and H-poor component to that in hot and "normal" component.

$$f_M(O) = \frac{(O/H)_2 \cdot n_2 \cdot f}{(O/H)_1 \cdot n_1 \cdot (1-f) + (O/H)_2 \cdot n_2 \cdot f}$$

Bibliography

[1] Acker, A., Cuisinier, F., Stenholm, B., Terzan, A., 1992, A&A, 264, 217

[2] Allende Prieto, C., Lambert, D. L., Asplund, M., 2001, ApJ, 556, 63

[3] Aller, L. H., Kaler, J. B., 1964, ApJ, 139, 1074

[4] Barker, T., 1978, ApJ, 219, 914

[5] Barlow, M. J., Liu, X.-W., Péquignot, D., Storey, P. J., Tsamis, Y. G., Morisset, C., 2003, IAU Symp. 209, 373

[6] Bastin, R. J., Storey, P. J., 2006, IAU Symp. 234, 369

[7] Bohlin, R. C., 1996, AJ, 1996, 111, 1743

[8] Borkowski, K. J., Harrington, J. P., Tsvetanov, Z., Clegg, R. E. S., 1993, ApJ, 415, 47

[9] Brown, R. L., Mathews, W. G., 1970, ApJ, 160, 939

[10] Chesneau, O., et al. 2007, A&A, 473, 29

[11] Davey, A. R., Storey, P. J., Kisielius, R., 2000, A&AS, 142, 85

[12] Ferland, G. J., Korista, K. T., Verner, D. A., Ferguson, J. W., Kingdon, J. B., Verner, E. M., 1998, PASP, 110, 761

[13] Fernández, R., Monteiro, H., Schwarz, H. E., 2004, ApJ, 603, 595

[14] Garnett, D. R., Dinerstein, H. L., 2001, ApJ, 558, 145

[15] Gonçalves, D. R., Ercolano, B., Carnero, A., Mampaso, A., Corradi, R. L. M., 2006, MNRAS, 365, 1039

[16] Gruenwald, R., Viegas, S. M., 1995, A&A, 303, 535

[17] Guerrero, M. A., Manchado, A., 1996, ApJ, 472, 711

[18] Hill, G. J., et al. 2008, Proc. SPIE, 7014, 257

[19] Hyung, S., Aller, L. H., 1995a, MNRAS, 273, 958

[20] Hyung, S., Aller, L. H., 1995b, MNRAS, 273, 973

[21] Iben, I. Jr., Kaler, J. B., Truran, J. W., Renzini, A., 1983, ApJ, 264, 605

[22] Kingdon, J. B., Ferland, G. J., 1995, ApJ, 450, 691

[23] Kwitter, K. B., Henry, R. B. C., 1998, ApJ, 493, 247

[24] Liu, X.-W., 1998, MNRAS, 295, 699

[25] Liu, X.-W., 2003, IAU Symp. 209, 339

[26] Liu, X.-W., 2006a, in Planetary Nebulae beyond the Milky Way, ed. J. Walsh, L. Stanghellini, and N. Douglas (ESO, Garching bei München), 169

[27] Liu, X.-W., Barlow, M. J., Zhang, Y., Bastin, R. J., Storey, P. J., 2006b, MNRAS, 368, 1959

[28] Liu, X.-W., Danziger, J., 1993, MNRAS, 263, 256

[29] Liu, X.-W., Luo, S.-G., Barlow, M. J., Danziger, I. J., Storey, P. J., 2001, MNRAS, 327, 141

[30] Liu, X.-W., Storey, P. J., Barlow, M. J., Clegg, R. E. S., 1995, MNRAS, 272, 369

[31] Liu, X.-W., Storey, P. J., Barlow, M. J., Danziger, I. J., Cohen, M., Bryce, M., 2000, MNRAS, 312, 585

[32] Liu, Y., Liu, X.-W., Barlow, M. J., Luo, S.-G., 2004, MNRAS, 353, 1251

[33] Luo, S.-G., Liu, X,-W., 2003, IAU Symp. 209, 393

[34] Luo, S.-G., Liu, X,-W., Barlow, M. J., 2001, MNRAS, 326, 1049

[35] Marcy, G., et al. 2005, Prog. Theor. Phys. Suppl., 158, 24

[36] Mathis, J. 1995, Rev. Mex. Astron. Astrofis. Ser. Conf., 3, 207

[37] Moreno-Corral, M., de La Fuente, E., Gutiérrez, F., 1998, Rev. Mex. Astron. Astrofis., 34, 117

[38] Nandy, K., Thompson, G. I., Jamar, C., Monfils, A., Wilson, R., 1975, A&A, 44, 195

[39] O'Dell, C. R., Balick, B., Hajian, A. R., Henney, W. J., Burkert, A., 2002, AJ, 123, 3329

[40] O'Dell, C. R., Henney, W. J., Ferland, G. J., 2007, AJ, 133, 2343

[41] Peimbert, M., 1967, ApJ, 150, 825

[42] Peimbert, M., 1971, Bol. Obs. Tonantzintla Tacubaya, 6, 29

[43] Peimbert, M., Peimbert, A., Ruiz, M. T., Esteban, C., 2004, ApJS, 150, 431

[44] Peimbert, M., Storey, P. J., Torres-Peimbert, S., 1993, ApJ, 414, 626

[45] Peimbert, M., Torres-Peimbert, S., Luridiana, V. 1995, Rev. Mex. Astron. Astrofis., 31, 131

[46] Péquignot, D., Amara, M., Liu, X.-W., Barlow, M. J., Storey, P. J., Morisset, C., Torres-Peimbert, S., Peimbert, M., 2002, Rev. Mex. Astron. Astrofis. Ser. Conf., 12, 142

[47] Péquignot, D., Liu, X.-W., Barlow, M. J., Storey, P. J., Morisset, C., 2003, IAU Symp. 209, 347

[48] Reay, N. K., Atherton, P. D., 1985, MNRAS, 215, 233

[49] Rubin, R. H., 1989, ApJS, 69, 897

[50] Rubin, R. H., et al. 2002, MNRAS, 334, 777

[51] Seaton, M. J., 1979, MNRAS, 187, 73

[52] Shaw, R. A., Dufour, R. J., 1994, ASPC, 61, 327

[53] Smits, D. P., 1996, MNRAS, 278, 683

[54] Storey, P. J., 1994, A&A, 282, 999

[55] Storey, P. J., Hummer, D. G., 1995, MNRAS, 272, 41

[56] Tsamis, Y. G., Barlow, M. J., Liu, X.-W., Storey, P. J., Danziger, I. J., 2004, MNRAS, 353, 953

[57] Tsamis, Y. G., Walsh, J. R., Péquignot, D., Barlow, M. J., Danziger, I. J., Liu, X.-W., 2008, MNRAS, 386, 22

[58] Tylenda, R. 2003, IAU Symp. 209, 389

[59] Viegas, S. M., Clegg, R. E. S., 1994, MNRAS, 271, 993

[60] Wesson, R., Liu, X.-W., Barlow, M. J., 2005, MNRAS, 362, 424

[61] Zhang, C. Y., Kwok, S., 1991, A&A, 250, 179

Vita

Sehyun Hwang was born in Seoul, Korea on February 16, 1973, the son of Mr. Wonchul and Mrs. Wooboon Hwang. After graduating from Seoul National University with the highest distinction and receiving a Bachelor of Science degree in Astronomy, he obtained a Master of Science in Physics at the University of Wyoming. He applied to the University of Texas at Austin for enrollment in the astronomy program, was accepted, and started graduate studies in August, 2006.

Permanent address: 2425 Cromwell Circle, Apt. 1506
Austin, TX 78741

This thesis was typeset with LaTeX[†] by the author.

[†]LaTeX is a document preparation system developed by Leslie Lamport as a special version of Donald Knuth's TeX Program.